THESIS FOR THE DEGREE OF LICENTIATE OF ENGINEERING

Optical microscopy for monitoring liquids and nanoparticles inside nanofluidic channels

LOVA WILSKE

Department of Physics

CHALMERS UNIVERSITY OF TECHNOLOGY

Gothenburg, Sweden 2025

I

Optical microscopy for monitoring liquids and nanoparticles inside nanofluidic channels
LOVA WILSKE

Cover:
Illustrative representation of light scattered (in purple) from metal nanoparticles stationed in a nanochannel, and an induced phase shift to plane waves (in yellow) as they are transmitted through a nanochannel.

"Color is a drama in which there are only two actors, absorption and scattering. The great variety of colors arises from the many roles these two actors can play."

- *Craig F. Bohren*

Abstract

Nanofluidics constitutes a promising platform for studying properties of single particles in a confined environment. Single particle studies can provide unique insights into the fields of chemistry, biophysics, and material science, that extend beyond the knowledge gained when ensembles of billions of particles, with either slightly, or sometimes vastly, varying properties, are studied simultaneously. Robust and high-precision characterization methods are required to realize studies of single particles. In this context, optical microscopy, which can be employed to detect tiny changes of the refractive index of a liquid or solid medium, constitutes a non-invasive approach allowing to monitor the flow of particles and liquids through nanochannels with, potentially, high spatial and temporal resolution. In this work, I examine two techniques – dark-field scattering microscopy and cross-grating wavefront microscopy – and successfully determine solute concentration within sub-100 nm nanofluidic channels using them. While dark-field provides higher signal-to-noise ratios within my studies, cross-grating wavefront microscopy provides the benefit of quantitative measurements of liquid refractive index below the diffraction limit. Additionally, I investigated the light scattering signatures of metal nanoparticles contained within nanofluidic channels and found peculiar relationships between particle dimensions and their visibility when observed in a dark-field microscope. I developed a theoretical framework to aid the interpretation of scattering signals from such combined channel-particle systems.

List of Appended Papers

This thesis is based on the following appended papers:

Paper I: Lova Wilske, Joachim Fritzsche, Barbora Špačková, Bohdan Yeroshenko, and Christoph Langhammer. Light Scattering Contrast Inversion of Single Metal Nanoparticles inside a Nanofluidic Channel. (In manuscript)

Paper II: Lova Wilske, Baptiste Marthy, Puvaneswari Teluchina-Appadu, Joachim Fritzsche, Guillaume Baffou, and Christoph Langhammer. Cross-Grating Wavefront Microscopy of Individual Nanofluidic Channels. (In manuscript)

My contribution to Appended Papers

This thesis is based on the following appended papers:

Paper I: I performed all measurements and data analysis. The samples were fabricated together with Joachim Fritzsche. I derived the model with initial support from Barbora Špačková. I made the figures of the manuscript and co-wrote the first draft.

Paper II: I performed all experiments and data analysis together with Baptiste Marthy. I made the figures of the manuscript and co-wrote the first draft.

X

Contents

1 Introduction

Experimental and theoretical research have each contributed profoundly to advancing nanoscience. While theory provides a scaffold for understanding and predicting phenomena at the nanoscale, it is the careful eye of the experiment that grounds these insights into reality. In conventional experimental approaches involving nanoparticles and nanostructures, the underlying mechanisms of, for example, catalytic reactions, material properties, or biological processes, the result is often obscured by ensemble averaging, i.e., averaging the response of millions of individual contributions that, potentially, all could be slightly different. Single particle and single molecule experiments have therefore emerged as a powerful approach to close the gap between predictions and measurements at the nanoscale since, in particular, ab initio theoretical methods still are unable to treat ensembles of nanoparticles. To this end, over the course of the last two decades, substantial progress has been made in experimental techniques with single nanoparticle and single molecule resolution, such as plasmon-enhanced spectroscopy[1,2], optical and magnetic tweezers[3,4], transmission electron microscopy (TEM) in different forms[5–7], ionic conductance measurements through nanopores[8], and single-molecule fluorescence microscopy[9]. This has enabled – and to some extent even "made mainstream" – single-particle studies of site-specific reaction kinetics[10–12] and single protein and antibody binding event investigations[13], to name a few examples. Although these methods have opened new frontiers thanks to their impressive resolution, sensitivity and specificity, they still also face technical challenges related to resolution, scalability, and environmental compatibility, such as operation in technically relevant chemical environments, temperatures and pressures, as

well as compatibility with technically relevant materials, rather than only so-called simplified model systems.

Nanofluidics offers a particularly compelling platform in this context. Not only does it enable the study of *individual* particles, which can be confined, manipulated, and observed under highly controlled conditions inside nanofluidic structures, but it also allows researchers to explore fundamental physics emerging from fluid *confinement* to the nanoscale. Specifically, when fluidic systems are miniaturized below ~100 nanometers, their behavior diverges from bulk norms. For example, flow profiles deviate from classical predictions[14,15], viscosity of liquids inside such fluidic structures can change[16,17], and electrostatic interactions become dominant as characteristic dimensions approach the Debye length or the mean free path of solutes[18]. This relates to technically highly relevant questions like how do the porous structures of catalyst support materials influence a catalytic reaction, and what role does confinement play in biological processes? In this context, nanofluidic systems constitute a tool for precise, label-free single-particle or single molecule experiments to advance our understanding of, e.g., molecular transport[19], catalysis[20–22] and drug delivery[23,24], and a subject of investigation in its own right[25,26].

To study single particles and nanoscale phenomena within nanofluidic structures and devices, robust characterization tools are essential. To this end, a variety of established techniques including resistivity measurements[27,28], mass spectroscopy[29], chromatography[30], liquid-phase transmission electron microscopy[31], and fluorescence microscopy[32,33] have been employed to probe nanoscale processes and properties related to nanofluidics. While these methods offer valuable chemical, structural, and sometimes even kinetic

information about processes and particles inside nanofluidic structures, they often involve invasive sample preparation or lack the temporal or spatial resolution required to capture dynamic events in situ. For example, fluorescence microscopy has for decades been a dominating player on the scene of single nanoparticle and single biomolecule research. However, the technique suffers from photobleaching and requires chemical tagging by fluorophores that can perturb the system under study and, for example, potentially alter its biological activity[34,35]. To mitigate this shortcoming of fluorescence microscopy, so-called *label-free* optical microscopy methods are heavily studied, since they promise a non-invasive and very versatile means to study single molecules and nanoparticles that does not require labeling by fluorophores. In this thesis, I investigate the potential of two such label-free optical microscopy methods for studying liquids and nanoscale processes confined inside nanofluidic structures: dark-field microscopy and cross-grating wavefront microscopy (CGM).

In dark-field microscopy, a sample is illuminated at an oblique angle, allowing the light scattered from a nanoscale object in the focal plane to be collected and analyzed, while excluding the directly transmitted and reflected beam from detection[36,37]. A familiar everyday example is tiny scratches on the windshield of a car that become visible due to the scattering of light. Additionally, the scratches appear brighter when viewed in air than when submerged in water or oil. This effect similarly also happens with the fluidic systems I have worked with in this thesis (which, in essence, can be regarded as tiny scratches in glass) and is the result of the differences in the refractive index (RI) between the material that is scratched and its surrounding medium. By harnessing RI differences at the nanoscale, dark-field microscopy can, thus, detect sub-wavelength sized features and visualize

dynamic processes that appear on or inside such structures by measuring their light scattering properties. However, while dark-field microscopy is a particularly effective method for detecting strong and spatially isolated scatterers, it is limited when it comes to distinguishing signals from weakly scattering (and thus very small) structures in general, and in particular, when they are positioned in close vicinity of objects that scatter more strongly. To overcome these limitations, interference-based techniques have emerged as a powerful approach to capture weak scattering signals from, for example, single biomolecules. One of these approaches, interferometric scattering microscopy (iSCAT)[38], improves sensitivity by referencing the tiny amount of light scattered by single biomolecules or biological nanoparticles randomly attaching/detaching to/from a surface, as it interferes with the light scattered from the surface itself. Similarly, our group recently introduced nanofluidic scattering microscopy[39] (NSM), which relies on the interference between light scattered from a nanofluidic channel and the tiny amount of light scattered by a nanosized object, such as a single biomolecule, diffusing freely inside that nanochannel. In this way, NSM has been demonstrated to enable real-time, label-free detection of freely diffusing single biomolecules and provides access to molecular weight and hydrodynamic radius measurements.[39]

Apart from being a tool for studying biological particles and molecules as already demonstrated, NSM also holds promise for studying dynamic processes taking place on the surface of metal nanoparticles[22,40,41]. Some examples of such processes are ligand-surface interactions relevant in colloidal nanoparticle synthesis, catalytic conversion of reactants relevant in catalysis and morphology reconstructions due to outside stimuli. However, the optical properties of biological and metal nanoparticles are widely

4

different, i.e., for biological (dielectric) systems the interaction with visible light is mostly non-dispersive[42], whereas in metallic systems the interaction is dominated by the free electrons that give rise to plasmon resonances in the visible spectrum[43]. This increases the complexity of the interaction of light with a nanofluidic channel with a metal nanoparticle inside it, which is one of the focus areas of this thesis.

My interest in metallic nanoparticles originates from previous efforts of metal particle tracking within nanofluidic systems. Specifically, in some systems the particles were easily visible, whereas in other nanochannel-particle combinations similar metal particles were essentially completely invisible, when imaged in a dark-field microscope. These preliminary observations mean that within the Rayleigh regime (particle diameter $\ll \lambda$) the scattering intensity of a metal particle in a nanochannel does not necessarily increase with particle size (which it does when the particle is localized on an open surface or inside a homogeneous medium[43]), which I find counterintuitive, as scattering spectra from particles on an open surface are known to increase in intensity with diameter[44–46]. What poses an even more intriguing mystery is that sometimes metal particles can appear as dark spots inside a nanochannel and other times as bright ones. In Manuscript I, I resolve this mystery by combining theoretical and systematic experimental work that extends our understanding of the interaction of visible light with metal nanoparticles localized inside nanofluidic structures. Looking forward, this fundamental understanding will extend the applicability of the NSM method to metallic nanoparticles, which are of particular interest in, e.g., heterogeneous catalysis and nanoscale optical sensors.

As introduced above, phase-sensitive microscopy, such as CGM, is another interesting class of optical microscopy that can be used to study nanoscale objects and processes[47]. It relies on the fact that when light is transmitted through a medium, its phase will be distorted. The distortion is proportional to the RI and path length of the light travelling through the medium. Projected onto my work, this indicates that phase-sensitive microscopy could potentially be used to quantitatively determine the RI of the content of a nanochannel. In this context, CGM in particular constitutes a compact and sensitive method for measuring wavefront distortions, that has been gaining attention in the last years within the bio and photonics community, owing to its effectiveness at, e.g., measuring optically transparent living cells[48,49] and for its ability to characterize so-called optical metasurfaces.[50] In CGM, a cross-grating is placed in front of a camera sensor to spatially separate out first order diffraction patterns produced by the sample. Together with a reference measurement of the substrate material, wavefront images with a sensitivity of ~1 nm phase delay can be resolved. Although there are plenty of studies where wavefront techniques have been applied to microfluidic systems[51–56], they have never, to my knowledge, been employed to nanofluidics. One fundamental difference between imaging micro and nanochannels with CGM, is that they generally are on the opposite side of the diffraction limit – a nanochannel will therefore appear as a convolution of its own optical properties and the point spread function of the microscope system. In Manuscript II, we evaluate the potential of CGM to quantify local RI variations and visualize diffusion profiles across nanofluidic channels.

As I will discuss in this thesis in detail, together, NSM and CGM form a complementary toolkit for probing nanofluidic systems and nanoparticles in nanochannels by label-free non-invasive optical microscopy.

2 Nanofluidics

Nanofluidics is an umbrella term encompassing studies of flow at the nanoscale, generally, *within* nanostructures.[26] The term 'nanofluidics' was adopted around 25 years ago[57,58], as a sub-branch of microfluidics (which deals with fluid flow at the microscale). However, the interest in nanoscale flow properties extends further back in history than that. In this chapter, I will give a brief overview of the field of nanofluidics and its many branches and thereafter define my own position within that tree.
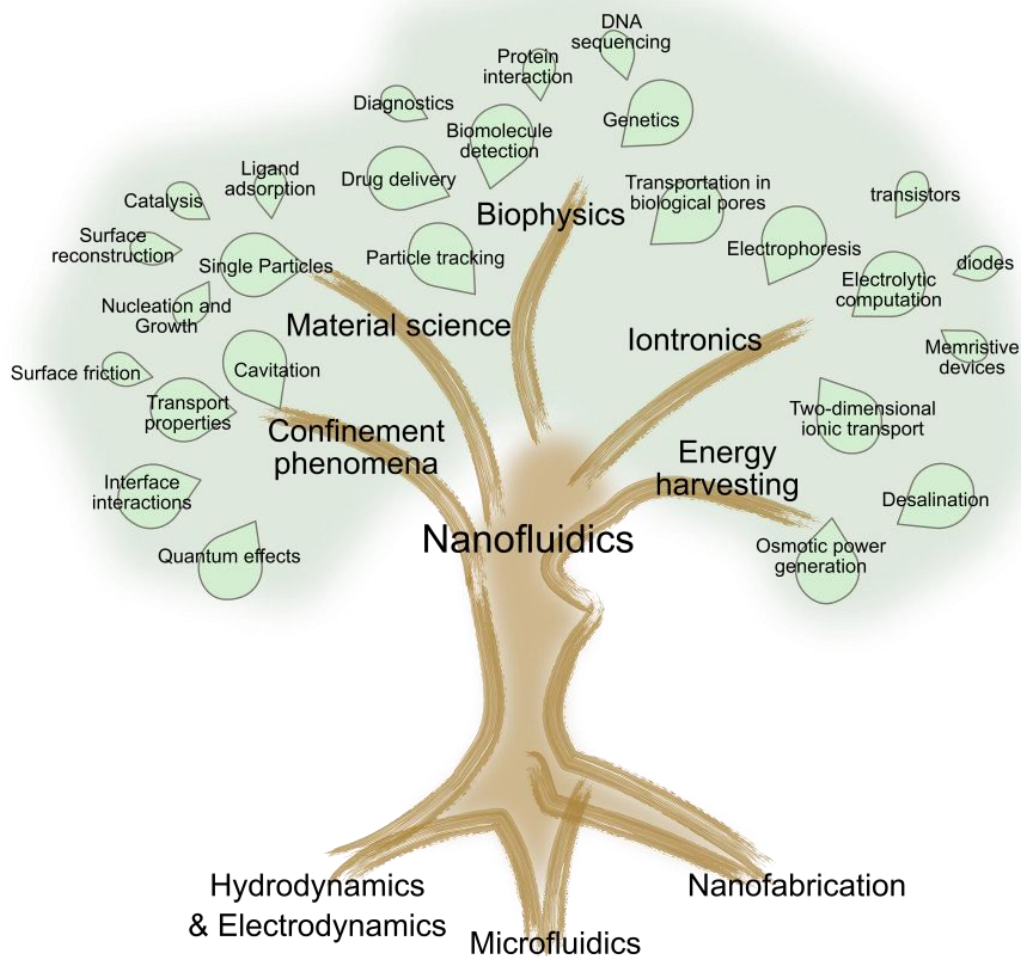

Figure 2-1. Roots and branches of the field of nanofluidics – an overview of the disciplines within nanofluidics and their origins.

The emergence of nanofluidic devices can roughly be traced to three different roots of disciplines; (i) downsizing of microfluidic systems, (ii) enabled by the development of nanofabrication techniques[59], and (iii) the prospect of experimentally probing effects related to hydrodynamics and electrokinetics at interfaces[25,26]. For the biologists and synthesis chemists within the microfluidics community, the birth of nanofluidics meant an extension of single particle studies and access to a new regime at smaller length scales.[60] For example, while the microfluidic length scale is comparable to eukaryotic cells[61], nanofluidics align with the dimensions of biological pores[62] that regulate molecular transport within cells. However, when fluids are confined to spaces smaller than 100 nanometers, a new physical regime is entered. At this scale, for example, the confinement becomes comparable to the Debye length, the distance over which electrostatic interactions are screened in a liquid. Consequently, classical bulk behavior breaks down for liquids confined at this scale, and surface effects and interface-molecule interactions become dominant[26].

Current nanofluidics research spans multiple, sometimes overlapping, domains. An overview of these domains is summarized in figure 2-1. One branch focuses on physics under confinement, with recent attention to quantum effects[63,64] in ultra-narrow channels. Other active disciplines deal with single particle studies contributing to material science, biophysics[65–68], and sensor applications[69,70]. Another more recently appearing branch of nanofluidics is iontronics, where the flow of ions through nanofluidic structures is explored as a potential complement, or alternative, to traditional electronics.[71–73] The prospect of harnessing energy from osmotic flow through membranes is also a relatively new addition to the family of nanofluidics.[74–76] Given this rich and expanding scope, it becomes clear that

nanofluidics means different things to different communities. The term may refer to many types of systems, i.e., nanopatterned channels spanning up to millimeter distances, solid-state or biological nanopores, nanopipettes[77], nanoslits, porous membranes, or nanofluidic systems made from carbon nanotubes[78] and 2D materials[79–81] like graphene and hexagonal boron nitride, to mention a few.

The nanofluidic platforms used in the experiments presented in this thesis, are based on in-house fabricated silicon-based fluidic chips with nanofluidic channels etched into the thermal oxide of a silicon wafer. Their design and micro- and nanofabrication will be presented in detail in the upcoming chapter. The fluidic chips have multiple inlets which allows the introduction of liquid solutions and particles. Mass transport within the chip is either accomplished via pressure driven flow or diffusion. The platform allows for both single particle studies and mapping of flow profiles in nanochannels spanning distances of tenths of micrometers.

3 Nanofabrication

Nanofabrication generally refers to the crafting of structures at the nanoscale on flat solid surfaces. This field of research combines disciplines from physics and chemistry to materials science and engineering and enables the making of devices and materials with rationally tailored properties. At its core, nanofabrication is about manipulating matter down to atomic or molecular precision, thus tailoring the physical, chemical, and biological properties of materials. This capability opens up a wide range of applications, spanning from electronic devices[82] and developing advanced medical therapies[83] to creating novel materials[84] with, for example, improved strength and conductivity. The practice and development of nanofabrication are motivated by the fundamental principle that materials exhibit unique behavior when their dimensions are reduced to the nanoscale, often due to quantum effects and increased surface area compared to the total volume of the system.[85] The techniques used in nanofabrication can be roughly divided into top-down and bottom-up approaches.[86] Top-down approaches involve shaping larger materials into nanoscale structures, while bottom-up methods assemble structures from individual atoms or molecules. The ongoing development of nanofabrication techniques, including lithography, etching, and self-assembly, continues to push the boundaries of what is possible and promises to transform numerous industries and drive future technological advances.

In this chapter, I describe the nanofabrication and design of the nanofluidic chips used in my work. I will explain why we use certain nanofabrication processes and materials in chip production and the different chip formats I have used.

3.1 Design and material considerations for nanofluidic chips

Our lab has a decades-long tradition of nanofluidics research.[87–89] Established chip designs and material selections were developed even before the work presented within this thesis began. While most design and material decisions are based on specific, rationally derived principles, certain aspects reflect historical precedents dating back to the initial exploratory phase of nanofluidics activities in the lab over a decade ago. The following section provides a comprehensive overview of the critical design, material, and manufacturing parameters of our nanofluidics chip development, considering both established principles and historical context.

Figure 3-1. Material structure of a chip cross section: structures are etched in a thermally grown silicon dioxide (SiO_2) film on a silicon wafer. The wafer is then thermally bonded to a lid of borosilicate glass to hermetically seal the fluidic structures and form enclosed "channels".

Our standard material for nanofluidic chips is a "sandwich" of a thermally oxidized silicon wafer with a thin SiO_2 layer terminating its surface into which the fluidic structures are fabricated, and a borosilicate glass wafer that is thermally bonded to the SiO_2 film to hermetically seal the fluidic structures and form enclosed "channels", as shown in figure 3-1. The use of silicon as a substrate is generally popular in the field of micro and nanofluidics[90], as

silicon is one of the most commonly used materials in nanofabrication and as most processes are compatible with it or have even been specifically developed for this material. All micro- and nanostructures on the chip, such as channels, inlets, and markers, are etched into the SiO_2 layer that is up to 2 µm thick. Working with silica-based channels comes with a number of benefits - SiO_2 is inert to many chemicals that may be necessary or interesting for experiments, it is biocompatible unlike metals, and it is hydrophilic unlike many plastics, which can be of great importance when filling small fluidic structures with water-based solutions.[91–93] Glass is also transparent, allowing optical microscopy-based measurements in the fluidic systems through the glass lids, as in focus of my thesis. The use of borosilicate as a lid, especially Borofloat 33, is based primarily on the fact that this glass and silicon (which constitutes the main body of our chips) have very similar thermal expansion coefficients.[94] This allows the two pieces of material to be bonded together in high temperature processes without the material stack being destroyed by excessive stress during cooling.

The simplest design of a nanofluidic chip consists of two microchannels with inlets at the ends and nanochannels connecting the two microchannels, as presented in figure 3-2 a). In our case, the microchannels typically serve solely to transport fluids from the inlets to the nanochannels, where the measurements then take place. Over the past decade, more complex variants of this simple chip design have been developed and deployed in our lab. Nevertheless, this simple design is perfectly adequate for many of our experiments. It also offers the major advantage over more complex systems that one can intuitively understand which flows arise in the system by applying certain overpressures at the inlets. However, in the field of microfluidics, which is much broader than the field of nanofluidics,

significantly more complex systems are often used. The main reason for this difference is that we typically only need to reliably fill our nanochannels with a specific fluid to conduct our experiments. In contrast, microfluidics often uses complex concepts to enable specific functions, such as fluid mixing or droplet formation[95].
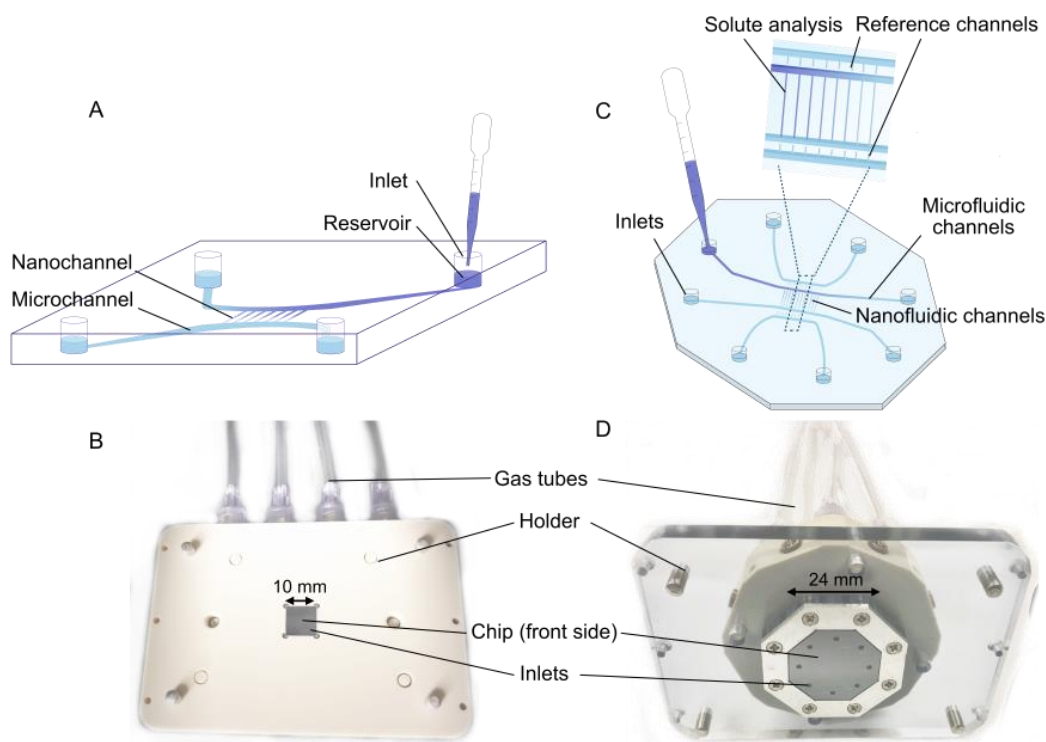

Figure 3-2. Two different chip designs: A chip with 4 inlets, 2 microchannels and an area with parallel nanofluidic channels that connect to the microchannels in the middle is illustrated in a). An image of the chip mounted in a holder is presented in b). An octagonal silicon chip with 8 inlets is depicted in c), with an inset of separate nanofluidic systems positioned in close vicinity of each other. The corresponding chip and holder are shown in d). The rectangular holder plates in b) and d) have the same area.

When designing a fluidic chip, there is no universal solution for its format, i.e., its lateral shape and size. Rather, multiple factors must be considered in each specific case and application, such as (i) the number of chips one gets per processed wafer, (ii) the required homogeneity of the structures on a chip

or between chips on one wafer, (iii) the required number of inlets, or (iv) the handleability of the chips and the components used with the chips, such as O-rings for sealing the chips to a holder. At the beginning of my work, various chip formats were already in use, two of which I have continued to employ in my experiments. One of them is a small 10×10 mm^2 chip with four inlets (presented in figure 3-2 a-b) and represents a compromise between increasing the yield of number of chips fabricated on each wafer, while still enabling reasonable practical chip handling. The second design features eight inlets, allowing experiments with three separate fluidic systems within the same field of view of an optical microscope. As illustrated in figure 3-2 c), four inlets in this design are employed to steer liquid flow in the middle section, while the remaining two pairs of inlets are reserved to carry liquids to dead-end nanochannels that in my experiments are used for cross-system *referencing*.

Introducing such *reference channels* is motivated by the fact that they can vastly improve the accuracy of optical measurements conducted over longer periods of time. Reference channels can, for example, be employed to account for fluctuations in light source intensity over time, as well as general drifts of the microscope like small changes of the focus.[96]

As earlier mentioned, the flow of liquid within the nanofluidic chips is controlled by applying pressure to the chip inlets. For this to work efficiently, the chip is mounted in custom-made holders, see figure 3-2 b) and d), that feature connections for one gas tube per inlet. The tubes are, in turn, connected to a pressure controller, which can be programmed to establish liquid flow within the chip.

15

All our fluidic chips are manufactured in-house in the Chalmers University cleanroom. This cleanroom is especially well equipped for the nanopatterning of surfaces, which indeed is critical for the fabrication of nanofluidic channels where the critical feature size is in the sub μm range. In particular, at Chalmers, we have extensive experience with electron beam lithography (EBL), which is why this is our method of choice for defining the nanochannels on our nanofluidic chips. All other processes needed for the fabrication of other features on our nanofluidic chips are, of course, just as important as patterning the nanochannels, but due to the larger dimensions of these structures, they fall into the realm of microfabrication and are carried out using different manufacturing techniques, which will be presented in the next section.
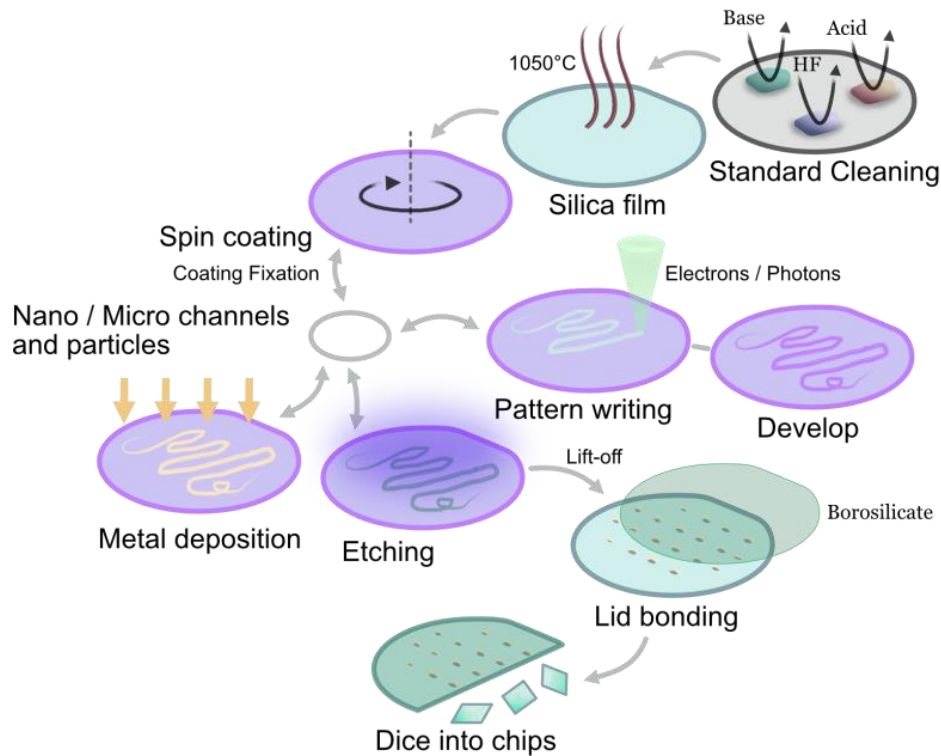
3.2   From Wafers to Nanofluidic Chips

Figure 3-3. Flow chart of the key micro- and nanofabrication steps of nanofluidic chips used in this thesis.

The nanofluidic chips are manufactured using silicon and glass wafers as the starting materials. All fluidic structures are etched into the thermal oxide grown on the silicon wafers, which thereafter are thermally bonded to Borofloat glass wafers to form a hermetic seal that encloses the fluidic structures and at the same time keeps them accessible for visible light-based microscopy. Finally, the processed wafers that host many repetitions of the same (or different) fluidic systems are diced into individual fluidic chips. This process is illustrated in figure 3-3 and involves the following steps:

We use 1 mm thick, 4-inch silicon wafers (100) as the starting material. We note that the (100) crystal orientation of the wafers is not critical for our application, i.e., also other Si crystals could in principle be used. The wafers are first cleaned using a standard cleaning process[97] (SC1, HF, SC2) to remove potential organic and inorganic surface contaminants. The wafer surfaces are then oxidized in water atmosphere at high temperatures (950–1050 °C) to a defined thermal SiO_2 layer thickness. The thickness of this oxide layer can be adjusted by oxidation time and temperature and depends on the application of the chip. An important aspect in our context is that interference occurs at the silicon-silicon oxide interface when such an oxidized wafer is irradiated by light[98], which can lead to undesirable strong oscillations in scattered light intensity as function of wavelength. A practical way to circumvent this "oscillation problem" is to make the oxide layer such that it is only slightly thicker than the depth of the nanochannels, i.e. ~100 nm.
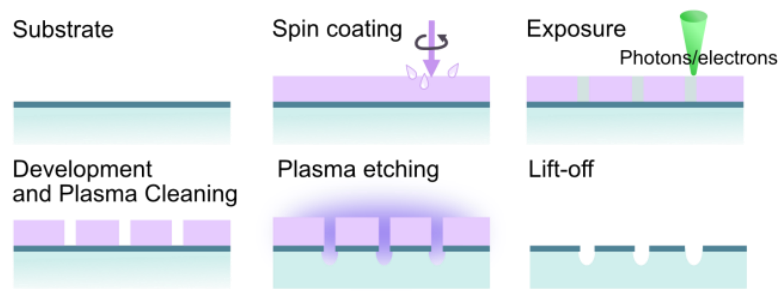
Figure 3-4. Photolithography/EBL processing steps for creating fluidic structures in the thermal oxide of a Si wafer substrate.

As the next step, we etch marks into the wafers that can be registered by both EBL and photolithography tools. For the rest of the processing, the fabricated marks serve as a reference system for aligning the structures created in the consecutive steps. We define the shapes of these marks in a resist layer using photolithography, such as direct laser writing, or in rare cases EBL, and transfer the defined pattern with dry etching into the wafers with fluorine-based plasma (CF_4). A generic process scheme for defining, developing and transferring a pattern is displayed in figure 3-4. The requirements for overlay accuracy between consecutive process steps can vary greatly. In most of our cases, overlay accuracy is not critical, as all components of the fluidic systems simply need to be interconnected, which can be easily achieved with generous structure overlaps of, for example, 5 μm. For such cases, one pair of marks per lithography process, as indicated in figure 3-5 in blue, is sufficient. However, for designs that require alignment of multiple nanostructures, special measures must be taken during mark fabrication. In Manuscript I, we present a chip design where plasmonic particles are fabricated (by EBL) directly into nanochannels, which in this particular case, required an overlay accuracy of 15 nm. To prevent pattern mismatches from

occurring in such cases, the marks must correspond as closely as possible to their nominal shape, have sharp etched edges, and be positioned as precisely as possible relative to each other. These requirements imply that in such cases, marks must be defined using the same lithography tool used for the steps where overlay accuracy is critical, i.e., EBL. Furthermore, the marks must be defined in high-resolution resist, similar to the processing of nanostructures. Finally, the marks must be defined for each individual chip, as shown in figure 3-5 in gray. Individual chip marks will minimize the time between registration of the markers and exposure of structures on that chip to reduce the influence of thermal drift of EBL tools.
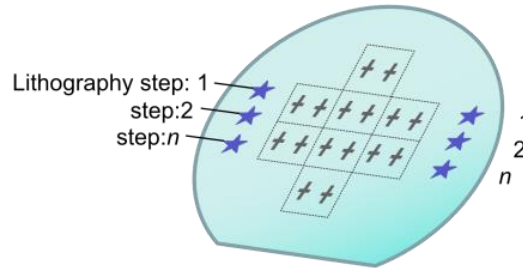

Figure 3-5. Schematic illustration of reference marks for lithography processes. For low pattern alignment accuracy, pairs of marks (indicated by blue stars) are sufficient. Higher accuracy (sub-100 nm) may be achieved by adding additional marks to each chip (as indicated by gray crosses). The shape of the marks must be adjusted to the tool, and each lithography step requires its own set of marks.

As a next step, using EBL, we define the nanochannel structures in a resist layer and then transfer them to the thermal oxide of the wafers using fluorine-based plasma, as summarized in figure 3-4. The channel depth can be tailored by adjusting the etching time. It is desirable to achieve low surface roughness of the channel walls, as this enables a smooth flow during experiments, and greatly improves the optical signal-to-noise for imaging. For particularly demanding low line edge roughness of the nanochannels, a resist with the

highest possible resolution is required; in our case, this is usually polymethyl methacrylate (PMMA). However, the etch resistance of PMMA in fluorine based plasma is rather low compared to other electron beam resists[99], which can lead to unwanted plasma exposure that may ruin the surface of the substrate. Therefore, it is often more appropriate to use resists with higher etch resistance but lower resolution, such as ethyl lactate based resists, provided the specific application of the nanofluidic chips allows it.
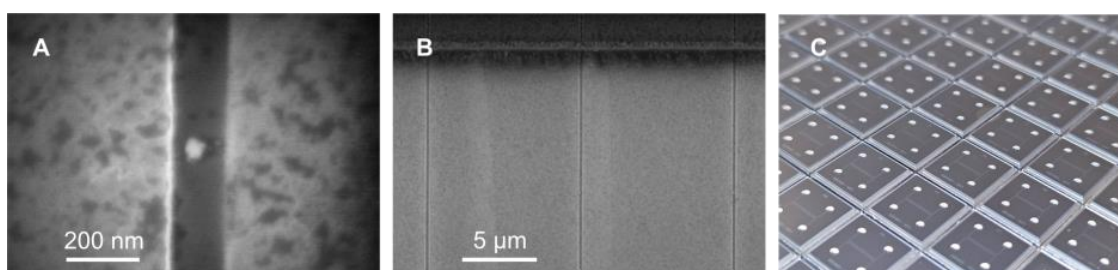
Figure 3-6. a) SEM image of a nanoparticle fabricated within a nanochannel. b) SEM image of nanochannels connected to a microchannel. c) Photograph of a pre-diced wafer comprising many identical 10×10 mm^2 nanofluidic chips with four inlets.

For experiments concerning nanoparticles within nanochannels, additional processing may be required. Particles can either be introduced by flushing and trapping colloidal nanoparticles at predefined positions using traps[40] or by nanofabricating them directly into the channel. The second option can be achieved by patterning a sacrificial layer through EBL and then depositing a layer of metal at a normal angle onto the sample. The mask is consecutively dissolved in a solvent, lifting off the metal layer except in the patterned regions. An example of such a sample is depicted in figure 3-6 a-b).

After first defining the structures using lithography steps outlined above, the nanochannels, microchannels and inlets are etched into and through the wafer, respectively, with deep reactive ion etching (DRIE). DRIE relies on two alternating plasma species[100] – one that protectively coats the wall side (C_4S_8) and another on etching in a mainly downward direction (SF_6) – to achieve purely vertical etching. After DRIE and before the processed wafers can be bonded to the Borofloat glass lid, careful cleaning of the wafer is required, as even small amounts of resist residues or other contaminants can lead to voids forming between the processed wafers and the bonded glass lids. This, in the worst case, can render entire chips unusable, for example, because liquid can leak out of the fluidic system if the lid is not perfectly bonded. Therefore, in preparation for the bonding process, we clean both lid and processed wafer in hot piranha solution and activate the wafer surfaces to be bonded in oxygen plasma, which has an additional cleaning effect. For chips with fabricated metal particles, piranha may be switched to less harsh chemicals, such as acetone. The wafers are then fusion-bonded to the glass, where the plasma-activated surfaces are first manually pressed together until they adhere as void-free as possible and then annealed for several hours near the glass transition temperature of the Borofloat lid (550 °C), which significantly increases the bonding strength and hermetically seals the fluidic systems. Finally, the bonded wafers are diced into individual chips, an example of which is shown in figure 3-6 c).

4 Scattering of Light by Small Particles

When light encounters a heterogeneity in space, such as a material boundary, a molecule, or a single elementary charge, it may interact with the material and set the elementary charges (electrons and protons) into an oscillatory motion. As the excitation attenuates, the energy is either absorbed (ultimately leading to the formation of heat) or converted into secondary radiation in a process known as scattering. If the scattering is elastic, light is simply redirected and maintains its initial energy. The probability of either route is governed by the scattering and absorption cross section of the illuminated object, that in turn is a consequence of the object's geometry, material, and surrounding environment.[101]

A blue sky on a clear day displays a prime example of *Rayleigh scattering* – elastic scattering of light by atmospheric molecules, such as N_2 and O_2 and H_2O, much smaller than the wavelength, λ. Since shorter wavelengths are more comparable to the molecule size, the process is more effective in the blue part of the spectrum, $I_s \sim \frac{1}{\lambda^4}$, causing the sky to appear blue to our eyes.
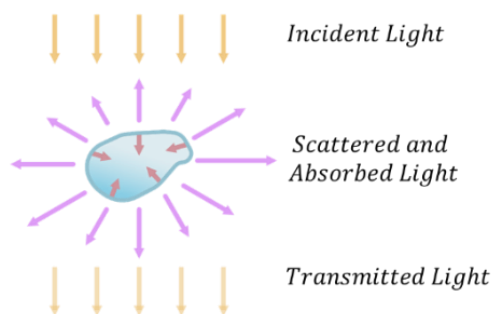

Figure 4-1. Scattering and absorption of light by an arbitrarily shaped particle.

When a particle is small in comparison to the irradiated wavelength, the irradiated field applied across the particle will be perceived as uniform, and the scattering of light will, thus, be dominated by dipolar radiation. However, the situation becomes far more complex as the particle size increases. We have now entered the regime of *Mie scattering*. In this regime, the field strength and direction will vary across the particle and thus form multiple modes within the particle, known as multipoles, which in turn affects its scattering properties.

The electromagnetic field of any system, regardless of the number of modes present, is governed by the solutions to Maxwells equations. However, in practice, analytical solutions are for most systems impossible to generate and one instead must rely on numerical electrodynamic calculations. The only systems for which there exists an exact analytical solution are the scattering of plane waves by either a spherical particle or an infinite cylinder. The corresponding theory was developed over 100 years ago through a series of collaborations and independent discoveries by Debye, Clebsch, Rayleigh, Lorentz and Mie, and is today commonly called Mie theory[102]. In Mie theory, the scattered field is described by the superposition of *all* possible normal modes, each weighted by the appropriate scattering coefficient for each mode. The coefficients are based on Bessel functions, which were initially developed to describe a very different phenomenon, i.e., the modes of vibration on a string[103].

In my experiments, I have illuminated nanostructures with unpolarized light and observed how certain parameters, such as nanostructure size, shape, surrounding medium and illumination wavelength affect its scattering response. In this chapter I will derive expressions and approximations for how their scattering responses can be estimated, and I will later use these

results to interpret my experimental data. The nanofluidic channels presented in the previous chapters were evidently rectangular in cross section, but if we want to analytically describe their scattering, it is more convenient to approximate them as homogenous infinite cylinders. Similarly, the disk-like metal nanoparticles I have worked with, I will approximate as ellipsoids.

4.1 Light scattering from a nanochannel in a dielectric matrix

The scattering cross section of a light scattering object, from here on denoted σ_s, provides a convenient measure when comparing the scattering response of different (nano)structures. Although it comes in units of m^2 that denotes an area, it is not an area in a purely physical sense like matter taking up space, but rather a virtual area proportional to the likelihood of light redirecting as it propagates in the vicinity of the particle. The scattering cross section measures the average flow of energy due to scattering (W_s) over a surface, Ω, far away from the scattering object.[101]

$$\sigma_s = \frac{W_s}{I_i} = \frac{1}{I_i}\int_\Omega \mathbf{S}_s d\Omega \qquad (4-1)$$

I_i is the incident light intensity and $\mathbf{S}_s$ the scattering contribution to the Poynting vector $\mathbf{S}$ (total flow of energy over a surface), which can be expressed as[101]

$$\mathbf{S}_s = \frac{1}{2}Re(\mathbf{E}_s \times \mathbf{H}_s^*) \qquad (4-2)$$

where $\mathbf{E}_s$ and $\mathbf{H}_s$ are the scattered electric and magnetic fields, respectively. In Mie theory developed for systems of infinitely long cylinders, $\mathbf{E}_s$ and $\mathbf{H}_s$ can be represented by a superposition of weighted cylindrical vector harmonics (CVH). The CVH-modes are generated by solutions to the Helmholtz equation ($\nabla^2 \psi + k^2 \psi = 0$) in a cylindrical coordinate system, and each mode signifies a different distribution pattern that the field can assume. The weights that govern the influence of each CVH-mode are called scattering coefficients, and they depend on the cylinder material, geometry, embedding medium and the incident field.

If we consider an incident wave vector following the coordinate system as depicted in figure 4-2, the polarization of the electric field of an incident plane wave can be divided into 3 categories – parallel to the incidence plane ($\hat{\mathbf{e}}_{i\parallel} = sin\zeta\,\hat{\mathbf{e}}_z - cos\zeta\,\hat{\mathbf{e}}_x$), orthogonal to the incidence plane ($\hat{\mathbf{e}}_{i\perp} = -\hat{\mathbf{e}}_y$), or somewhere in between. The third category can then be described by a linear combination of the two priors. Modes excited by orthogonal polarization applied along the diameter axis of the cylinder are referred to as *transverse electric modes*, TE for short. When an electric field with parallel polarization instead is applied to a cylinder, its magnetic counterpart acts along the cylinder diameter axis, giving rise to the *transverse magnetic mode* (TM). As scattering power is dependent on surface area, we therefore expect the TM mode, where the electric field is acting along the cylinder to contribute more scattering power than the TE mode, if a cylinder is illuminated by unpolarized light.
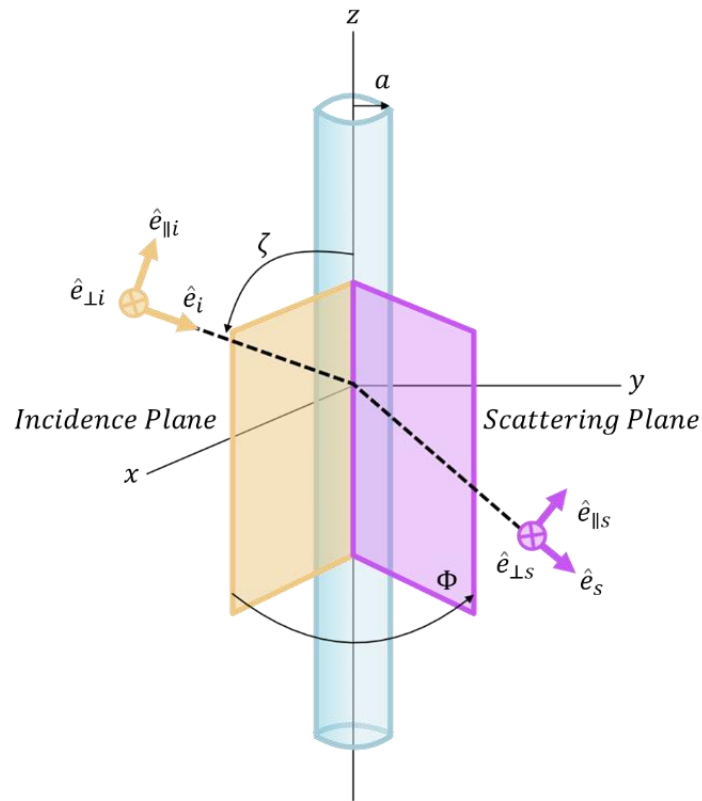
Figure 4-2. Scattering of light by an infinitely long cylinder. The angle of illumination, denoted by ζ, is defined as the angle between the z and x axis. The illumination can be decomposed into light polarized parallel and orthogonal to the incident field as indicated in the figure.

In addition to describing $\mathbf{E}_s$ and $\mathbf{H}_s$, the scattering coefficients can autonomously be employed to form σ_s for a system where every angle, Φ, of scattering around a cylinder is included. However, since σ_s of an infinitely long object is infinite (unless its scattering power is zero), we shall for now use the more convenient measure of σ_s divided by the physical cross section that incident light is projected upon – the *scattering efficiency* – to express the scattering response of the TM and TE modes respectively, as it is independent of the channel length L.[101]

$$Q_{s,TM} = \frac{\sigma_{s,TM}}{2aL} = \frac{2}{x}\left(\left|b_{0,TM}\right|^2 + 2\sum_{n=1}^{\infty}\left|a_{n,TM}\right|^2 + \left|b_{n,TM}\right|^2\right) \qquad (4-3)$$

$$Q_{s,TE} = \frac{2}{x}\left(\left|a_{0,TE}\right|^2 + 2\sum_{n=1}^{\infty}\left|a_{n,TE}\right|^2 + \left|b_{n,TE}\right|^2\right) \qquad (4-4)$$

where $x = ka$ is a size parameter, $k = 2\pi n_o/\lambda$ is the wavenumber, n_o the RI of the medium outside the cylinder, and a the radius of the cylinder. a_n and b_n denote the scattering coefficients governing the influence of the CVHs for each scattering mode, where $n = 1$ describes a radiating dipole, $n = 2$ a quadrupole, $n = 3$ an octupole, et cetera. a_n and b_n can be calculated for each incidence of polarization by satisfying field continuity at the cylinder surface.

So far, the only approximations made towards deriving an expression for the scattering cross section of our nanofluidic channels relate to the channel geometry and the assumption that the illumination is comprised of perfect plane waves. Although Mie theory could provide us with an exact solution, the (infinitely) many terms accounting for each multipole, and long expressions based on the notorious Bessel functions make it tedious to work with. Another motivation for searching for a simplified expression for σ_s, would be the prospect of extracting the polarizability of the cylinder, since this measure in combination with the polarizability of a different object would allow us to investigate interference effects within a two-object system, such as a metal nanoparticle inside a nanochannel, which I will deal with later in the chapter.

As stated in the introduction of this chapter, the main portion of the scattering power from an object much smaller than the incidence wavelength is

contributed by dipole radiation, and we shall from here on discard the higher order multipoles and only consider cylinders within the $2a \ll \lambda$, and $2am \ll \lambda$ limits. The relative RI, $m = n_c/n_e$, is the ratio between the RI inside the cylinder and the RI of the embedding medium. Within these limits, the scattering coefficients associated with the dipole radiation from an infinitely long homogenous cylinder illuminated by plane waves perpendicular to the cylinder axis ($\zeta = 90°$) can be approximated as[101]

$$a_0 \approx \frac{-i\pi x^4(m^2 - 1)}{32}, \quad b_0 \approx \frac{-i\pi x^2(m^2 - 1)}{4},$$
$$a_1 \approx \frac{-i\pi x^2}{4}\frac{m^2 - 1}{m^2 + 1}, \quad b_1 \approx \frac{-i\pi x^4(m^2 - 1)}{32} \qquad (4-5)$$

Within the limits of the approximation $a_{1,TM} = a_{1,TE}$ and $b_{1,TM} = b_{1,TE}$. It may also be noted that this approximation only can be employed for describing dark-field microscopy configurations where the channel is illuminated from the side of the channel and not parallel with it. With the scattering coefficients at our hands, we may now insert the expressions into equation (4-3), and (4-4), and if the higher order terms are discarded, we obtain the following expression for the approximate scattering efficiencies

$$Q_{s,TM} \approx \frac{\pi^2 x^3}{8}(m^2 - 1)^2 \qquad (4-6)$$

$$Q_{s,TE} \approx \frac{\pi^2 x^3}{4}\left(\frac{m^2 - 1}{m^2 + 1}\right)^2 \qquad (4-7)$$

From the formulas it is evident that RI differences between the cylinder (that represents a nanochannel that I use in my experiments) and its embedding medium affects the magnitude of Q_s – the larger the difference in RI, the

29

larger scattering power is generated. Secondly, we may observe that the scattering efficiency, presented for a cylinder with a 10 nm radius in figure 4-3, is larger for shorter wavelengths, which is in line with Lord Rayleigh's predictions made over 100 years ago.
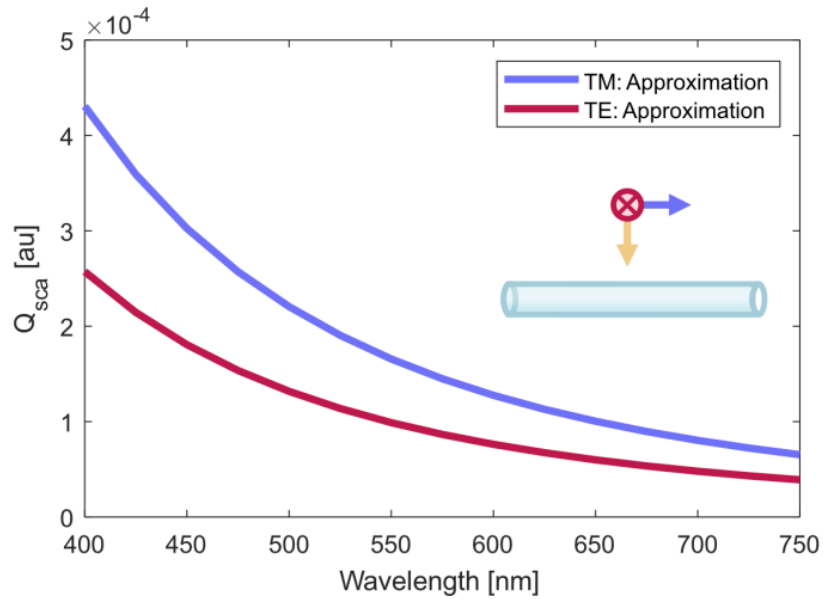

Figure 4-3. Scattering efficiency spectrum for perpendicular illumination of plane waves onto an infinitely long homogenous cylinder of radius a = 10 nm filled with water (n_c= 1.33) and embedded in silica (n_e = 1.46)[104].

At this stage, we may now combine the contribution of TE and TM polarization to represent unpolarized light, which I have used in my experiments. To retrieve σ_s, the scattering efficiency is multiplied with the physical cross section ($2aL$) along an arbitrary length of the cylinder, and we thus get

$$\sigma_s = 2aL\frac{1}{2}\left(Q_{s,TM} + Q_{s,TE}\right) = \frac{A^2 k^3 L}{4}(m^2 - 1)^2\left(\frac{1}{2} + \frac{1}{(m^2 + 1)^2}\right) (4-8)$$

where $A = \pi a^2$. By rearranging the factors, σ_s may be expressed such that the polarizability, α_c, of an infinitely long cylinder of radius a can be extracted

$$\sigma_s = \frac{k^3}{4} L \left| A(m^2 - 1) \left(\frac{1}{\sqrt{2}} + \frac{1}{(m^2 + 1)} \right) \right|^2 = \frac{k^3}{4} L |\alpha_c|^2 \qquad (4-9)$$

This will be important for estimating the scattering response of a two-object system, which will be investigated in section 4.3.

4.2 Scattering of metal nanoparticles

Metals can be described as crystalline materials containing a "sea" of free electrons that are delocalized across the structure. The mobile nature of the electrons affects the response of the metal as it is exposed to light. For example, when a particle of any material is illuminated by light, the electrons within the material will be excited and start to oscillate. What distinguishes metal (and dielectric) particles is their ability to sustain resonances – a phenomenon governed by the natural frequency of the electrons in a metal particle. Such resonant electron excitations are known as localized surface plasmon resonances (LSPR)[43], and their properties are tied to the dielectric function of the metal, the particle size, shape, and the surrounding medium. To this end, Michael Faradays investigations of gold colloids in 1850s have been celebrated as pioneering the field of plasmonics. However, the knowledge of how to work metals into nanoparticles has been around since the medieval era, where nanoparticles were mixed with glass to produce windows and goblets of vibrant colors.

In the following section, I will derive an expression for the scattering cross section of metal ellipsoids from the solutions of the so-called quasi-static approximation.
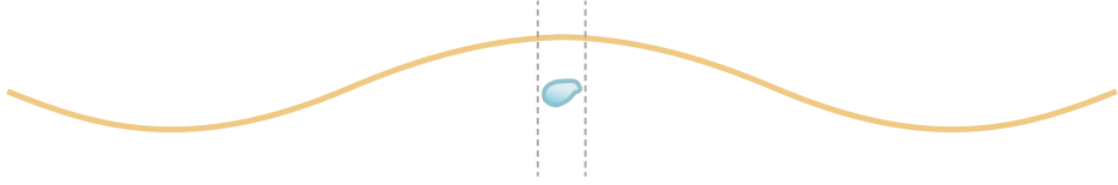

Figure 4-4. Particles that are much smaller than the wavelength of incoming light perceive the incoming field as uniform.

When the particle size is much smaller than the wavelength, as illustrated in figure 4-4, the phase changes of the applied electric field across the particle will be neglectable, and we may treat the system as a particle in a uniform field that varies with time (quasi-static approximation). In an electrostatics approach, the electric field, given by $\mathbf{E} = -\nabla\Phi$, can be calculated by solving the Laplace equation ($\nabla^2\Phi = 0$), provided the following 3 conditions are fulfilled; 1) the potential (Φ) must be finite at the origin of the particle, 2) far away from the particle the potential will be unperturbed, and 3) the electric field is continuous at the particle surface. For a homogeneous spherical particle of radius a, and dielectric function $\varepsilon(\omega)$, embedded in a non-absorbing, isotropic medium of dielectric constant ε_m, the solution to the Laplace equation in the surrounding medium, given an applied field $\mathbf{E}_0 = E_0\hat{\mathbf{e}}_z$, can be expressed as[43]

$$\Phi_m(r,\theta) = -E_0 r cos\theta + \frac{\varepsilon(\omega) - \varepsilon_m}{\varepsilon(\omega) + 2\varepsilon_m} E_0 a^3 \frac{cos\theta}{r^2} \qquad (4-10)$$

where r is the distance from the particle origin, and θ the angle from $\hat{\mathbf{e}}_z$. The first term corresponds to the applied field, while the second term resembles

an electric dipole. The dipole is associated with an induced dipole moment, which is proportional to the applied field

$$\mathbf{p} = \boldsymbol{\varepsilon}_{\mathrm{m}} \alpha \mathbf{E}_0 \qquad (4-11)$$

Here, α is the polarizability, a parameter describing how easily polarized a particle is once a field is applied and it is given by

$$\alpha = 4\pi a^3 \frac{\varepsilon(\omega) - \varepsilon_m}{\varepsilon(\omega) + 2\varepsilon_m} \qquad (4-12)$$

So far, we have only considered a static electric field. However, in a system where a particle is illuminated by plane waves, we must allow the field to vary over time, which will cause the dipole to oscillate.

$$\mathbf{p}(\mathrm{t}) = \boldsymbol{\varepsilon}_{\mathrm{m}} \alpha \mathbf{E}_0 e^{-i\omega t} \qquad (4-13)$$

If the frequency, ω, of the incoming field matches the natural frequency of the particle such that $\varepsilon(\omega) = -2\varepsilon_m$, a plasmon resonance arises. Such plasmon excitation will lead to secondary radiation – scattering. By treating the sphere as an ideal dipole in a time-dependent varying field, the scattering cross section becomes

$$\sigma_s = \frac{k^4}{6\pi} |\alpha|^2 \qquad (4-14)$$

The approximations we have gone through have – so far – been "unnecessary" since for calculating the scattering cross section of a *spherical*

33

particle we need to go no further than Mie theory. However, the approach of polarizability allows us to extend our calculations to include also ellipsoidal particles[105] which can serve as good approximations of metal nanoparticles that can be fabricated by nanolithography techniques, such as disks or rods[44–46]. If we have an elliptically shaped particle with radii $a_1 \leq a_2 \leq a_3$, the polarizability can be expressed as[101]

$$\alpha_j = V \frac{\varepsilon_p - \varepsilon_m}{\varepsilon_m + L_j(\varepsilon_1 - \varepsilon_m)} \qquad (4-15)$$

Here $V = 4\pi a_1 a_2 a_3 / 3$ is the volume, and L_j is a geometrical factor (see figure 4-5), custom for when the particle is placed within a field parallel to one of its principle axes: $j = 1$, 2, and 3. $j = 1$ designates the major axis (the axis along radius a_1) and $j = 3$ accounts for the minor axis (parallel to a_3).

$$L_j = \frac{a_1 a_2 a_3}{2} \int_0^\infty \frac{dq}{(a_j^2 + q)\sqrt{(a_1^2 + q)(a_2^2 + q)(a_3^2 + q)}} \qquad (4-16)$$

For any ellipsoid, the sum of the geometrical factors must be equal 1 ($L_1 + L_2 + L_3 = 1$), and it therefore follows that the geometrical factors of a sphere along any axis equal 1/3. If we substitute $L_j = 1/3$ in equation 15 for elliptical polarizability, we retrieve an expression identical to the polarizability of a sphere stated in equation 4-12.

The particles fabricated and studied in my experiments, i.e. disks and cylinders, do somewhat resemble spheroids, which are a subclass of ellipsoidal particles. Spheroids are distinguished by having at least two equal radii, and include spheres, prolates and oblates. Prolates are watermelon

shaped particles where $a_2 = a_3$, while oblates got two major axes ($a_1 = a_2$) and resemble the shape of pancakes of various fluffiness. To understand the interplay of aspect ratio and polarizability, L_j is presented as a function of eccentricity (the degree of spheroidal distortion) in figure 4-5. When L_j is increased, the polarizability, and hence also the scattering power radiated from a particle, is reduced. Figure 4-5 confirms that scattering power will be maximized for a particle if polarization is applied along its major axis.
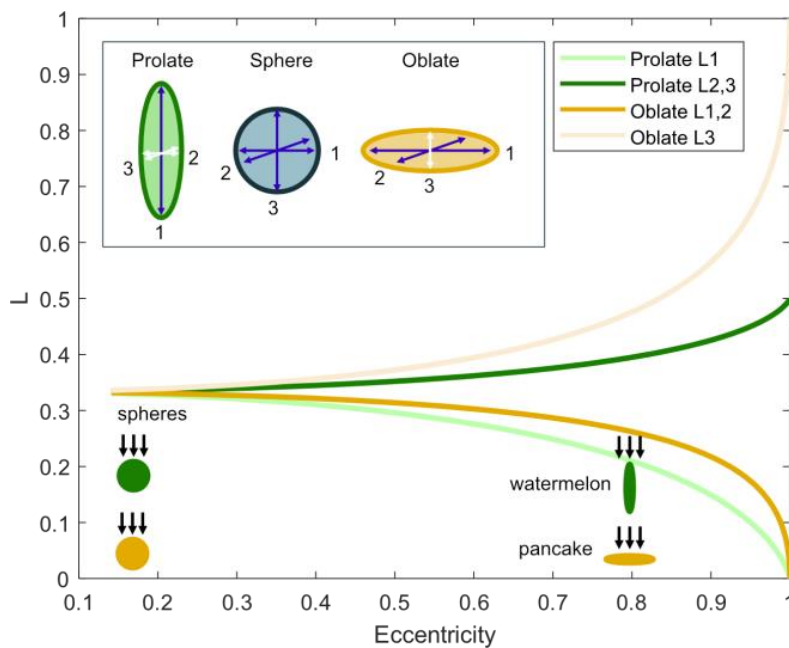

Figure 4-5. Geometrical factors of prolates, oblates and spheres as a function of eccentricity ($\sqrt{1 - a_3^2/a_1^2}$). The index announces which principal axis the electric field is applied parallel to. The black arrows indicate the direction of illumination corresponding to L_2 and L_3 for a prolate ("watermelon") and L_1 and L_2 for an oblate ("pancake").

If a field is applied at an angle, the contribution of polarization along each principal axis needs to be considered for describing the total polarizability of the particle.

$$\alpha = \sum_{j=1}^{3} \frac{\left|\mathbf{E}_{i,j}\right|}{\left|\mathbf{E}_{i,t}\right|} \alpha_j \qquad (4-17)$$

where $\mathbf{E}_{i,j}$ is the field applied parallel to axis j and $\mathbf{E}_{i,t}$ is the total initial field.

Until now, we have modeled the nanoparticles as ideal dipoles subjected to a uniform static electric field. However, this quasi-static approximation becomes increasingly inaccurate as the particle size grows. According to equation 4-11, a dipolar resonance of a sphere occurs as $\varepsilon_p = -2\varepsilon_m$. Nonetheless, it is well established that LSPRs are influenced not only by the material and medium permittivity but also by the particle's size and geometry. To address discrepancies in the scattering spectra of small particles, we thus employ the modified long wavelength approximation (MLWA), which incorporates finite-size effects, such as radiative damping and dynamic depolarization. Radiative damping increases rapidly with particle size, leading to enhanced energy loss through re-radiation of light. This effect reduces the strength of the induced dipole moment and results in a broadening of the plasmon linewidth. Dynamic depolarization arises from the spatial phase retardation of the electromagnetic field across the particle, due to the non-negligible ratio of particle size to incident wavelength. This phase non-uniformity causes a redshift of the plasmon resonance as the particle size increases.[106,107] These corrections lead to a more accurate description of the optical response of intermediate-sized plasmonic nanoparticles and yield a modified expression for the dipolar polarizability

$$\alpha_{MLWA,j} = \frac{\alpha_j}{1 - i\dfrac{k^3}{6\pi}\alpha_j - \dfrac{k^2}{4\pi a_j}\alpha_j} \qquad (4-18)$$

By substituting α_{MLWA} into equation 14, we may now express the spectrum of the scattering cross section for any small particle. Figure 4-6 shows the scattering cross section spectrum calculated by employing MLWA for gold and platinum spheroids supported on a silica surface ($\varepsilon_m = (\varepsilon_{air} + \varepsilon_{SiO2})/2$). As expected, the angle of incidence affects the spectra, and when a field is applied parallel to both the major and minor axis as in figure 4-6 a), two separate features are visible in the spectrum.
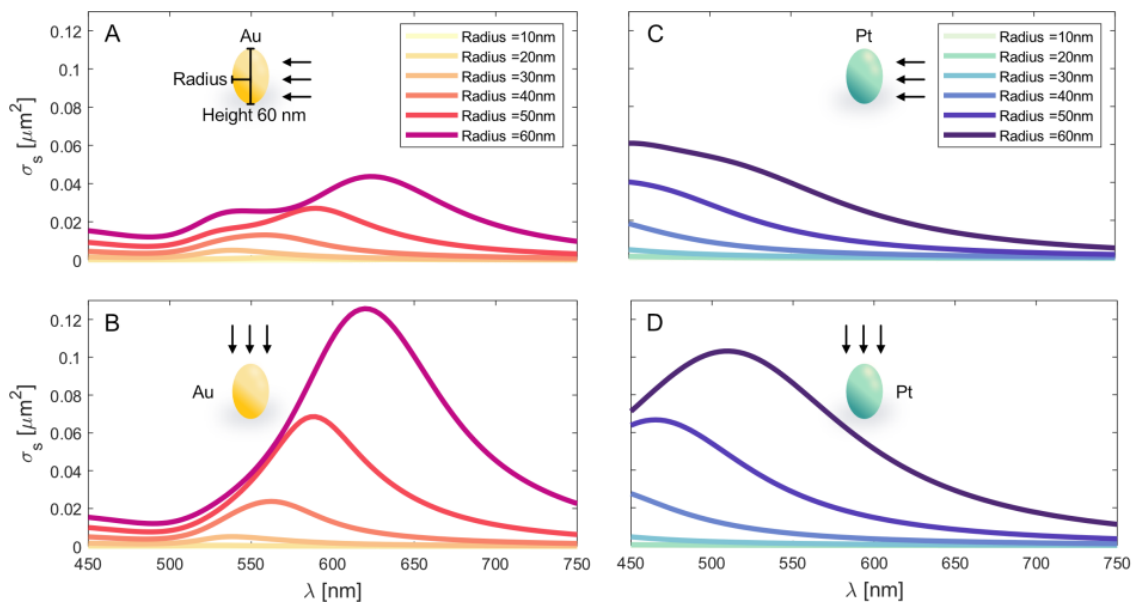

Figure 4-6. Scattering spectra of gold (a-b) and platinum (c-d) spheroids of height 60 nm in air and supported on silica ($\varepsilon_m = (\varepsilon_{air} + \varepsilon_{SiO2})/2$). The spheroidal particle is illuminated by unpolarized light in a direction illustrated by black arrows. The dielectric functions of gold and platinum were taken from Johnsson and Christy[108] for Au and from Werner[109] for Pt, respectively.

4.3 Predicting the scattering spectrum of a metal particle embedded in a nanochannel

Expressions for the scattering cross section have been derived for two distinct systems; each approached from a different theoretical perspective. First, a

nanochannel was modeled as an infinite cylinder, and its scattering efficiency was analyzed using the Mie theory framework. The scattering cross section was subsequently obtained by introducing a parameter L, representing the length over which the scattering efficiency is evaluated. In the second case, the scattering cross section of a metallic spheroidal particle was derived by modeling the particle as an ideal dipole within the quasi-static approximation. To understand the optical response of a metallic nanoparticle positioned in a nanofluidic channel I develop an expression for the scattering cross section of a two-object system where a metallic particle modelled as a spheroid is localized inside a nanochannel modelled as a cylinder. Such understanding may enable tailoring of nanoparticle visibility that further can facilitate the detection of particles in nanofluidic channels or guide the interpretation of dynamic changes of such particles or the sensing of variations in a liquid inside a nanochannel surrounding a particle inside said channel. Additionally, such a model could support the design of nanofluidic systems with tailored embedded particle optical properties through parameter tuning.

If an ellipsoidal particle is placed within a cylindrical channel and illuminated, both objects will scatter light. Observed at a distance, i.e. in the far field, the waves will interfere. This interference will contribute to the total scattering intensity as

$$I_{s,tot} = I_{s,c} + I_{s,p} + I_{s,int} \qquad (4-19)$$

where $I_{s,c}$, $I_{s,p}$, and $I_{s,int}$ is the scattering intensity attributed to the channel, particle, and the interference between the two, respectively. The cylinder and particle contributions can be retrieved by multiplying their scattering cross sections with the incident light intensity. However, we must yet find a way to describe the interference between them.

One way to approach this type of interference, that has previously been employed in the NSM framework[39], is to consider the *effective* polarizability within the space occupied by a molecule and the cylinder. However, adding the contribution of particle and cylinder in a joint effective polarizability is not entirely straightforward, as the units of the cylinder (m^2) and particle (m^3) polarizability do not match. Adjustments to the form of the analytical expression describing the scattering cross section and polarizability are therefore required for at least one of the two objects. Since the scattering spectrum of a metallic particle due to LSPR is more complex than the scattering spectrum of a nanochannel, I have chosen to preserve the analytical expression for the polarizability of a metal nanoparticle in the MLWA framework and rework the expression for the cylinder to obtain the same units for both systems. To do so, I will derive an analytical expression where a particle and a piece of cylinder *together* are described as an ideal dipole. As a first step to do so, I rearrange the factors in the expression for the scattering cross section of a cylinder given in equation 4-9 above to obtain

$$\sigma_{s,c} = \frac{k^4}{6\pi} \left| \sqrt{\frac{3\pi}{2}} \frac{A\sqrt{L}}{\sqrt{k}} (m^2 - 1) \left(\frac{1}{\sqrt{2}} + \frac{1}{m^2 + 1} \right) \right|^2 \qquad (4-20)$$

This expression alters the units of α_c to match the units of the polarizability of an ideal dipole in a quasi-static field [m^3]. Yet, this still leaves us with the mathematically uncomfortable $\sqrt{L}/\sqrt{k}$ - factor within α_c. To mitigate this, we ask ourselves what distance L that is relevant for $\sigma_{s,c}$ to describe the coupled cylinder-particle system at the position of the particle. While the cylinder is considered infinitely long, the particle occupies a volume whose span is shorter than the diffraction limit of light. As the diffraction limit of

light depends on the wavelength, it is reasonable to mathematically describe the particle-cylinder system over a distance that incorporates a single diffraction limited spot and adjust this length dynamically over the light spectrum. If we choose $L = k^{-1}$, and substitute $k = L^{-1}$ the cylinder polarizability over the diffraction limited spot becomes

$$\alpha_c = \sqrt{\frac{3\pi}{2}} AL(m^2 - 1)\left(\frac{1}{\sqrt{2}} + \frac{1}{m^2 + 1}\right) \qquad (4 - 21)$$

and we may now define an effective polarizability for the total system

$$\alpha_{tot} = \alpha_c + \alpha_p \qquad (4 - 22)$$

where α_p is the polarizability of a metal particle. The total scattering cross section for a particle within a cylinder observed over $L = \lambda/2\pi n_o$ then becomes

$$\sigma_{s,tot} = \frac{k^4}{6\pi}|\alpha_{tot}|^2 \qquad (4 - 23)$$

which can be expanded into the scattering cross sections of the cylinder and the particle, respectively, plus a remaining term that represents the interference between the two

$$\sigma_{s,tot} = \sigma_{s,c} + \sigma_{s,p} + 2sign(\alpha_c \alpha_p')\sqrt{\sigma_{s,c}\sigma_{s,p}'} \qquad (4 - 24)$$

,

where α_p' and $\sigma_{s,p}'$ are the real part of the particle polarizability and cross section, respectively.
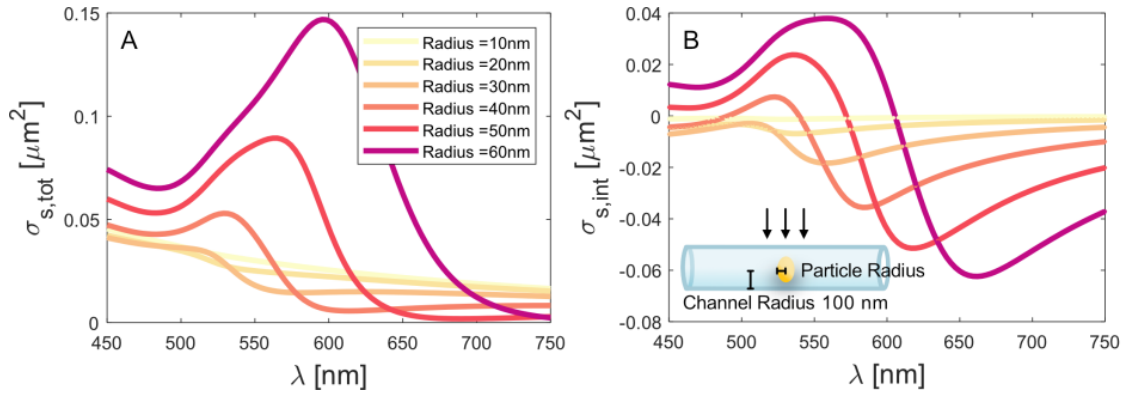
40

Figure 4-7. Calculated scattering spectra of gold spheroidal particles with varying radii and constant height of 60 nm localized in an air-filled cylinder with radius 100 nm embedded in a dielectric medium (silica) with RI 1.46[104] using the model developed in the text is presented in a). The cylinder is illuminated by unpolarized light incident perpendicular to the cylinder axis, as shown in the inset in b). The interference term ($2sign(\alpha_c\alpha'_p)\sqrt{\sigma_{s,c}\sigma'_{s,p}}$) spectra for the same systems are presented in b).

The total scattering cross-section spectrum for gold spheroids of various widths localized in an air-filled cylinder with 100 nm radius embedded in a silica matrix calculated using the framework developed above is presented in figure 4-7 a) together with the corresponding the interference term spectra of the same system in figure 4-7 b). We note that the scattering spectrum spectrum resembles a mix between the two objects, where the plasmon peak of the metal particle is heavily blue shifted due to the added interference term. It should also be noted that the cylinder presented in the spectra in figure 4-7, has a radius of 100 nm. This means, it has a dimension for which a$<<\lambda$ no longer 100 % strictly holds, and the calculated spectra therefore should be seen as a rough approximation only. That said, I chose this specific size to mimic the dimensions of my nanofabricated nanofluidic channel samples that I use in my experiments, such that comparisons between theory and

experiments can be performed in the upcoming chapter, at least at a qualitative level.

5 Optical Microscopy below the Diffraction Limit

Your eyes provide vision by letting incoming light propagate through the transparent cornea, the pupil, and a lens that focuses rays onto the retina. In daylight, the pupil spans roughly 5 mm, which corresponds to an angular resolution of 1.22 * 600 nm / 5 mm ≈ 0.008° for orange light. This allows the human eye to distinguish features down to about 35 μm at a viewing distance of 25 cm – fine enough to notice the texture of a grain of sand or the striations in a strand of hair. But far more lies beyond this natural limit. Microscopy has transformed our ability to perceive and analyze the micro- and nanoscopic world. Since the invention of the optical microscope in the 17th century[110], continuous advancements – from compound lenses to fluorescence labeling – have made it a versatile and indispensable tool across fields, such as biology, chemistry, and materials science. However, the resolving power of optical microscopy is inherently constrained by the *diffraction* of light. As described by Ernst Abbe[111] in the late 19th century, the smallest resolvable detail in a diffraction-limited optical system is approximately half the wavelength of the irradiated light – typically in the range of 200 to 300 nanometers for visible wavelengths. This limitation stems from the wave nature of light. When a point object is imaged through a circular aperture, it does not appear as a sharp dot but is instead spread out into an Airy pattern: a central bright spot surrounded by fainter concentric rings. This pattern defines the system's point spread function (PSF), and any image captured by the microscope is effectively a convolution of the true structure with this function. As a result, the image of a nanoparticle or a nanochannel is not a perfect representation of the object but rather a blurred proxy shaped by the PSF – blurring that ultimately sets the spatial resolution limit of the system. The finer the PSF, the better the system can distinguish

closely spaced features. Conversely, as features approach or fall below the diffraction limit, their images merge and become indistinguishable.

While the diffraction limit imposes a fundamental boundary on conventional optical imaging, several strategies can be employed to circumvent or work within its constraints. One approach is to extract more information from the diffraction-limited spots themselves – for instance, by analyzing their full *optical volume* rather than relying solely on intensity maxima. Another approach involves exploiting *interference*, allowing us to magnify and extract weak optical signals from otherwise hidden features. In this chapter, I will explore how these principles are applied in two distinct optical setups: dark-field microscopy and wavefront microscopy. I will present experimental results from studies of the optical signal associated with liquid exchange in nanofluidic channels acquired with the respective microscopy approach and also provide data on the scattering signature of systems of nanofluidic channels with plasmonic particles within.

5.1 Dark-Field Microscopy

When a tiny scratch on the windshield of a car is illuminated with sunlight it becomes vibrantly visible despite its tiny size. This is due to the phenomenon of light scattering, which similarly can be used to study surfaces with nanosized grooves, channels or particles. To do so, so-called dark-field microscopy, where illumination is performed at an angle while scattered light from the plane in focus is collected at a different angle, free of the transmitted or reflected beam,[37] is widely used.
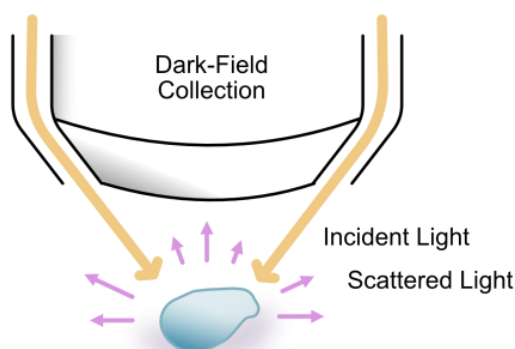
Figure 5-1. Schematic of a dark-field microscope objective for EPI-illumination (not to scale). Light illuminates a sample at an angle through a ring objective and the scattered light in the upward direction is collected along the objectives center axis. None of the directly irradiated and/or reflected light is collected in this way.

A dark-field microscopy configuration using a dry (i.e., no oil immersion) long-distance ring illumination objective is illustrated in figure 5-1. At the focus point, light illuminates the sample in the shape of a cone. In the previous chapter, I concluded that the intensity of scattered light from an infinite cylinder (and thus a nanofluidic channel) is proportional to its scattering cross section, which in turn is determined by the RI of the medium within the cylinder and the RI of the dielectric matrix the cylinder is embedded in (which in our case is silica, $n =1.46$[104]). This dependence of the intensity of light scattered from such a cylinder on the RI of the liquid inside it is demonstrated experimentally for a single nanofluidic channel with rectangular cross section with dimensions 250×350 nm^2 in figure 5-2. I let a salt solution ($n =1.358$) diffuse into a water filled channel ($n =1.332$) from one side. From each frame in the time series, an image of a water filled channel, acquired before the salt solution was introduced, is subtracted to generate a *differential scattering image*. In this way, scattering intensity

changes caused by a tiny alteration of RI of the liquid inside the channel appear more pronounced.
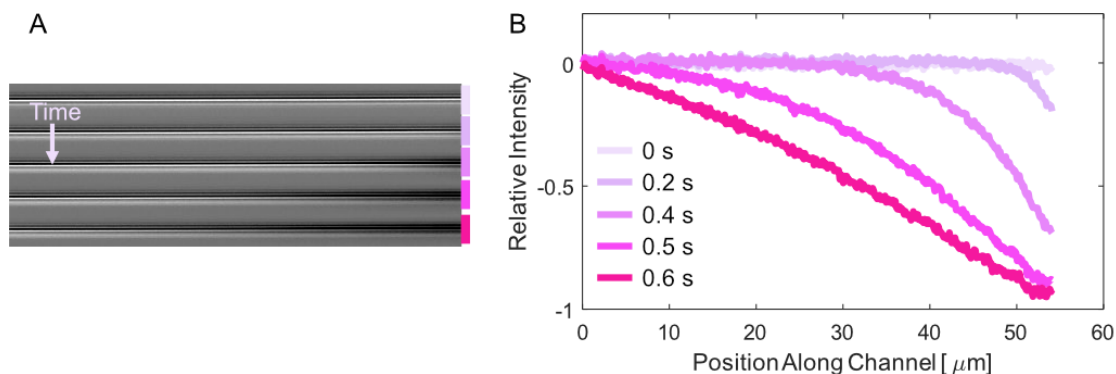

Figure 5-2. a) Differential dark-field images of a single nanochannel (dimensions 250×350 nm^2) where a 3 M NaCl solution is diffusing into an initially water-filled channel. A white light LED was used as light source. The scattering intensity along a 52 μm section of the channel changes once the NaCl solution is introduced. The corresponding change scattering intensity along the channel is presented in b). Each measurement in b) corresponds to the vertical summation of pixel count of a time series of frames (9 fps) of the kind presented in a).

The tracking of RI changes using dark-field scattering microscopy has been extensively used by our group to quantify RI changes in liquid-filled nanofluidic channels[22,96] or when performing surface passivation[39] within channels. In order to map out the limit of detection (LoD) in terms of how small RI changes that can be resolved, I have conducted dark-field measurements on NaCl solutions of known concentration (10-750 mM) that I flushed through a nanofluidic system, see figure 5-3. This time, the channels used and displayed in figure 5-3 have a cross-sectional dimension of 90×90 nm^2. To achieve as high LoD as possible, I applied the following data treatment protocol:

i)   I define a region of interest around a channel containing the first liquid (water) as shown in figure 5-3 a).

ii) I perform a linear background subtraction along the channel (within the defined region) for each row of pixels separately, to construct channel scattering intensity profiles across the channels. Figure 5-3 b) displays the average profiles across the 4 channels depicted in Figure 5-3 a). I define the scattering intensity, I_{water}, of each channel as the integration of its scattering intensity profile (or profiles).

iii) I carry out the same procedure for an image where the second liquid (NaCl solution) has replaced the first. I_{NaCl} is the integrated scattering intensity profile when the channels are filled with NaCl solution. I_{water} and I_{NaCl} along one channel is depicted in figure 5-3 c). It is important that the field of view is unaltered between the measurements of the two liquids, as the intensity may vary across the field of view (which is the case in figure 5-3 a)) due to potential sample tilt that can distort the focus.

iv) To account for these variations, I normalize the scattering intensity shift between the two liquids to the scattering intensity of the water filled channel according to

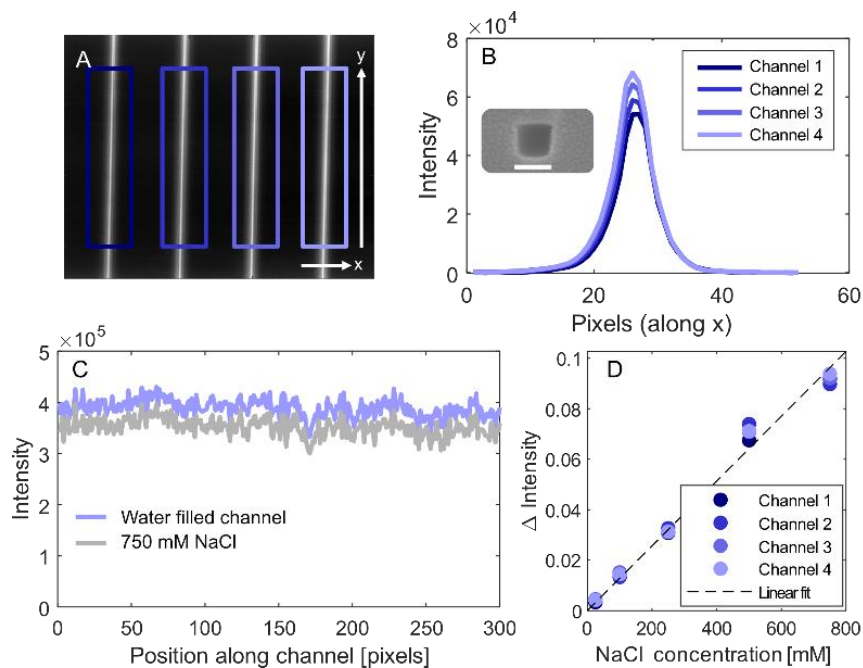$$\Delta I = \frac{I_{water} - I_{NaCl}}{I_{water}}. \qquad (5-1)$$

Figure 5-3. Four identical water-filled nanofluidic channels (90×90 nm² cross-section area) imaged with dark-field scattering microscopy are displayed in a). From the regions marked in different shades of purple, profiles of the measured scattering intensity across the channel (x-direction) for each channel can be constructed and are depicted in b). The inset displays a cross-sectional SEM image of a channel used. Scalebar 100 nm. The intensity variations along one channel (y-direction) of integrated intensity profiles are presented for a water and a 750 mM NaCl solution filled channel in c). In d), the scattering intensity difference of NaCl-solution filled channels for different NaCl concentrations (ranging from 10 mM to 750 mM) normalized by the scattering intensity of the corresponding water-filled channel, is shown. The dashed black line corresponds to a linear fit.

By applying this procedure, measurements of ΔI for 4 identical channels of cross sections 90×90 nm², presented in figure 5-3 d), show that water and NaCl solutions of concentrations ranging from 10-750 mM are distinguishable. The observed intensity shift between water and 10 mM NaCl was only 0.4 %. The concentration difference and the induced scattering

48

intensity difference are linearly dependent, which in turn demonstrates a correlation between concentration difference and RI of the solution inside the nanochannel. The results will be further discussed below and compared with similar measurements obtained through wavefront microscopy that I will introduce in the next section.

Having established the scattering intensity change of a nanochannel caused by liquid exchange, I will now turn my attention to the optical response of a channel containing a metal nanoparticle. In order to systematically study the influence that the particle dimension exerts on the particle's own scattering signature within the channel, a simple system composed of nanodisk arrays with size gradient was nanofabricated with a "nanotrench" (i.e., a nanochannel without lid) using EBL, see figure 5-4 a). The nanotrenches are nanofabricated into a PMMA film spin coated onto an oxidized silicon wafer and are aligned along the nanodisk array. The RI of PMMA and silica are nearly identical, and the optical response of this simple system should therefore be similar to a real nanofluidic system fabricated into silica and enclosed by a glass lid. Since it is open, however, it is possible to, e.g., take SEM images of the particles to determine their size.

To record the scattering intensity profiles of these systems, I inserted wavelength narrow band filters transmitting 500, 600, and 700 nm $\pm$ 10 nm, respectively, in the light collection pathway of the dark-field microscope to compare different parts of the spectrum. The results are shown in figure 5-4 b-d). Interestingly, the optical appearance of the particles with respect to the nanotrench alone varies from dark to bright as a function of their radius, as well of the used narrow band filters. This can conceptually be understood as an interplay between the light scattered by channel and the particle by means of interference. Using the theoretical framework presented in Chapter 4, the

relationship between scattering intensity and particle dimensions is qualitatively reproduced quite well, see figure 5-4. The graphs on the left display the experimentally obtained scattering intensity at certain wavelength, while the corresponding the analytically modeled total scattering cross section, σ, for the combined particle-cylinder system is presented on the right. The discrepancies between measurement and calculation can be explained by differences in respective configuration and the made approximations in the model. For instance, the particles in the experiment are 60 nm high disks and the nanotrenches are rectangular with $140{\times}200$ nm^2 cross section and no lid, while the model uses perfect metal spheroids (of height 60 nm) and cylindrical channels with a circular cross section, embedded in a homogenous medium. The height of the fabricated particle is determined by the metal deposition thickness, and the nanotrench depth by the thickness of the PMMA film. SEM analysis was employed to determine the particle diameter and nanotrench width.
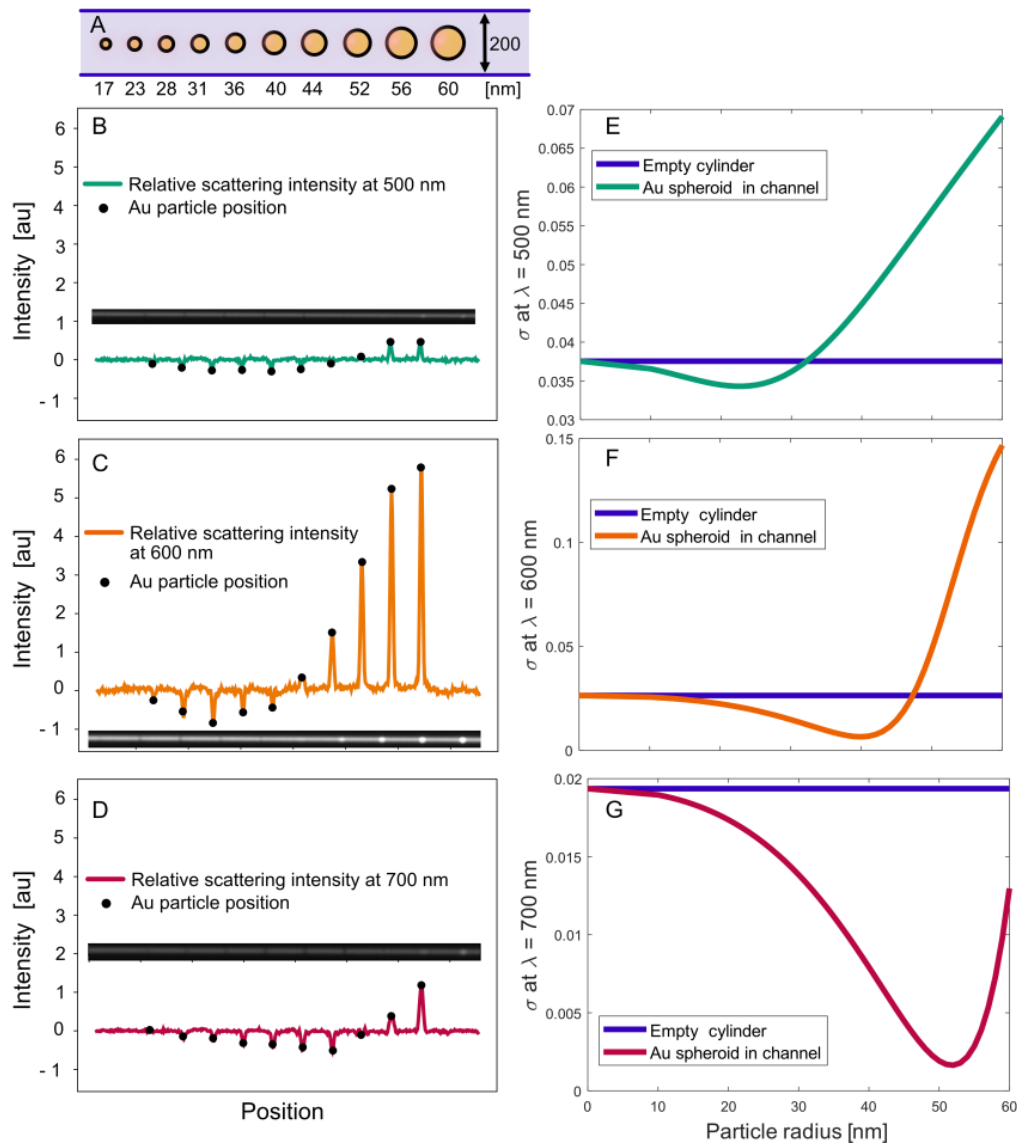
Figure 5-4. a) illustrates a system comprised of a size gradient array of nanodisks placed within a PMMA nanotrench. The trench diameter and particle radii are given in nm and were determined by SEM analysis. b-d) displays dark-field scattering images of the corresponding system measured at different wavelengths – 500, 600, and 700 $\pm$ 10 nm respectively. The intensity along the horizontal direction of the images minus the intensity solely attributed to the trench is presented in each graph. The position of the particle is indicated by black circular markers. In the panels on the right (e-g), the total scattering cross section calculated for all particles of varying radii within a cylindrical channel of 200 nm diameter using the model developed in chapter 4.3 is presented.

The angle of illumination constitutes another difference between my model and the experiment. The configuration used in the experiment illuminates the sample at a 50° angle from all directions trough the ring illumination objective, while the model only considers illumination at normal incidence. To qualitativly compare the difference ortogonal and parallel illumination with respect to the nanochannel, an aperture with two side slits, as depicted in figure 5-5 a), was placed in front of the objective to block out the majority of light, see figure 5-5 b). By turning the aperature, the influence of selected angles can be isolated, revealing distinctly different scattering signatures as the Au nanodisk array inside the nanotrench is imaged. As presented in figure 5-5 c), ortogonal illumination of the nanotrench results in a high scattering intensity of the trench that makes the particles apear as dark diffraction-limited spots, while illumination at an angle parallell to the trench almost cancels the scattering by the trench completely, whereas the particles themselves, due to their centrosymmetric disk shape, retain a strong scattering and appear bright. Hence, the interplay of light scattered by the nanotrench and the particles upon change of illumination direction results in a "contrast inversion" from the particles appearing bright to appearing dark, as well as from the nanotrech being very bright to completely invisible.
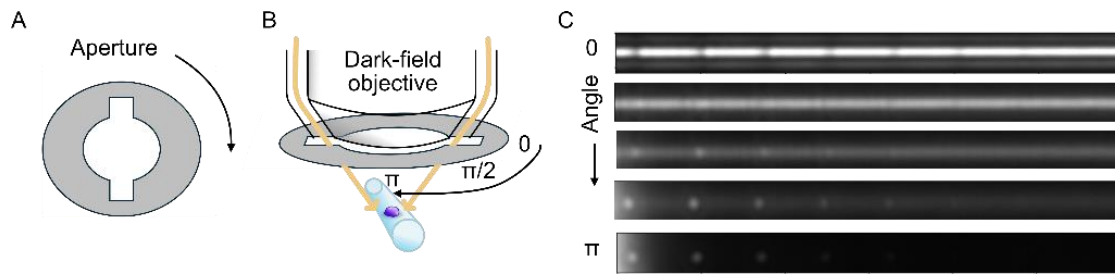
Figure 5-5. An aperture, as illustrated in a), was placed in front of the illumination pathway, controlling the illumination direction. By turning the aperture, as shown in b), the sample can be illuminated at selected angles. In c), a series of dark-field scattering images of an array of Au nanodisk particles (same as in Figure 5-4) placed within a nanochannel (200×70 nm^2) is displayed as function of the angle of aperture opening in regard to the channel direction, starting from orthogonal to the channel direction (top image) to parallel to the trench (bottom).

To summarize, in this chapter, I have investigated the influence of nanoparticle geometry and material, of nanochannel geometry, of RI of the medium inside the nanochannel, and of the illumination angle and wavelength on total scattering cross section of a nanoparticle inside a nanochannel, as obtained from dark-field scattering microscopy. The data and theory presented within this thesis and in Manuscript I provide a blueprint for how to understand and engineer the light scattering properties of a metal nanoparticle inside a nanofluidic channel.

5.2 Cross-Grating Wavefront Microscopy

While scattering-based microscopy methods have proven powerful for detecting RI changes at the nanoscale, they are not the only optical microscopy approach available for this purpose. When light is transmitted through a medium with an RI different from its surroundings, it is not only scattered but also experiences a shift in phase, as depicted in figure 5-6. These phase shifts alter the wavefront of the transmitted light, offering a complementary route for detecting small variations in RI of the medium that might otherwise be challenging to detect through intensity-based measurements alone.

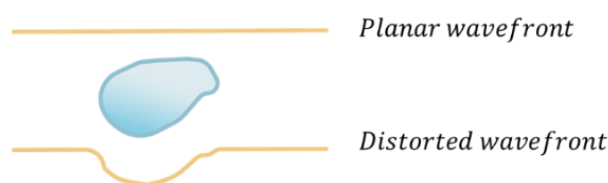*Planar wavefront*

Distorted wavefront

Figure 5-6. A plane wave is distorted as it is transmitted through an object.

Phase-sensitive microscopy, often termed quantitative phase microscopy (QPM), has been explored primarily within biological contexts, where transparent or weakly scattering samples, such as cells, pose challenges for traditional bright-field microscopy imaging because of the weak light-matter interactions in the visible spectrum[112]. Cells, though almost invisible in intensity-based imaging, introduce measurable phase changes in the light they transmit due to their internal RI variations and their RI contrast compared to cell culture medium[48]. Techniques such as digital holographic microscopy[113], spatial light interference microscopy[114], and diffraction phase microscopy[115] have become standard tools in biological research for

visualizing and quantifying these phase shifts.[116,117] Additionally, wavefront sensing using devices like Shack-Hartmann sensors has been adopted in fields ranging from adaptive optics to biomedical imaging[118]. QPM and wavefront sensing have also proven to be useful tools for characterizing processes within microfluidic systems, enabling label-free detection of cells[51–54] and droplets[55,56] through their induced phase shifts. These studies demonstrate the potential of phase-based methods for monitoring dynamic processes in fluidic systems. However, their use has so far been limited to *microscale* structures, where features are large enough to be spatially resolved, i.e., are above the diffraction limit. Importantly, however, the use of QPM techniques to liquids confined in the *nanoregime* and structures smaller than the diffraction limit of visible light, such as my nanofluidic channels, is widely unexplored.

Within the field of QPM methodologies and wavefront microscopy, in recent years, so-called cross-grating wavefront microscopy (CGM), which is based on quadriwave lateral shearing interferometry (QLSI)[48], has gained attention as a compact and sensitive method for wavefront sensing[47,119,120]. The technique was introduced to the optics community in the early 2000[121] by two French groups lead by Primot and Chanteloup, as an alternative to Shack-Hartman-sensors for wavefront sensing applications, and its use was later extended to the realm of wavefront microscopy[48] by Bon et al. In 2020, it was demonstrated by Baffou et al. that CGM can be employed to characterize the complex polarizability of nanoparticles[122]. For the interested reader, I recommend the following review by Baffou[50], for the historical records on the development of CGM and an in-depth description of the working principle of the technique.
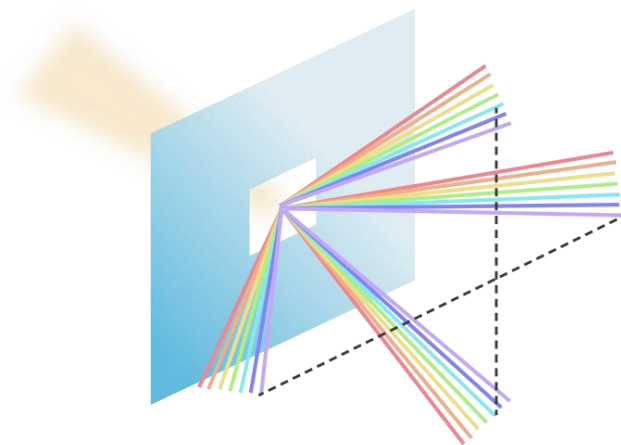
Figure 5-7. White light is diffracted as it is transmitted through a small quadratic aperture. Here, only the ±1 orders of diffraction maxima are shown.

In CGM, which is the terminology I use from here forward, a cross-grating is employed to analyze the wavefront of incoming light. The cross-grating is made of a two-dimensional array of small quadratic apertures, that upon illumination will diffract light, as depicted in figure 5-7. The phase of the diffracted light is dependent on the thickness of the material in which the aperture is embedded in. By alternating the "aperture thickness" in a pattern resembling the structure of a chessboard, all orders of diffraction are effectively canceled out by interference, apart from ±1, resulting in a "quadriwave" emerging from each aperture. Collectively, the quadriwaves form an interference pattern, known as *interferograms*, which holds spatial information about the incoming wavefront.

In a CGM set-up, see figure 5-8 a), a cross-grating is placed in front of a sensor of a CMOS/CCD-type camera, spatially separating the first-order diffraction patterns produced by a sample. These patterns form an interferogram, from which distortions in the wavefront can be extracted by comparing the sample interferogram to a reference interferogram, as shown

in figure 5-8 b). The reference interferogram is typically obtained from an empty region of the substrate of the sample, close to the object of interest. A narrow-band, non-coherent light source and precise calibration of the distance between the cross-grating and the camera sensor are required to obtain sensitive, speckle-free interferograms. If the camera housing prevents mounting of the cross-grating directly on top of the camera sensor, a relay lens can be used to project the image on the required plane[50].
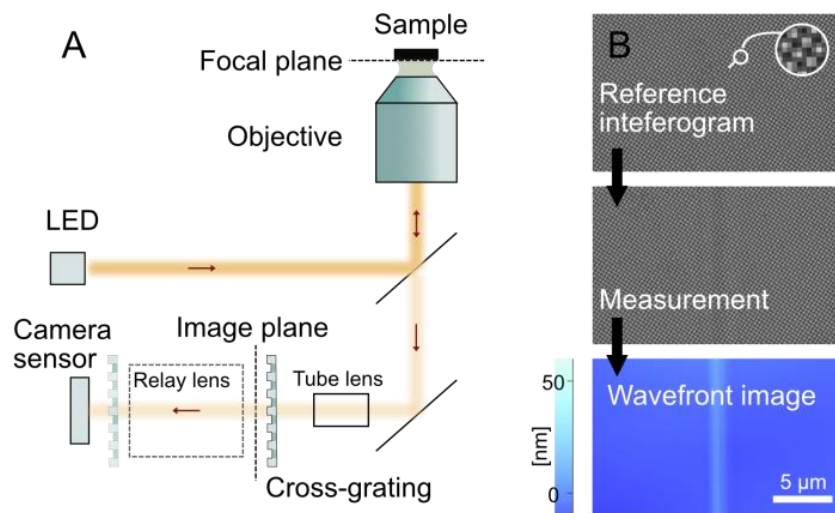

Figure 5-8. a) A schematic illustration of a cross-grating wavefront microscopy set-up. b) Two interferograms – a measurement and a reference – are acquired to form a wavefront image. The inset in the reference interferogram shows the characteristic diffraction pattern produced by a cross-grating.

A wavefront image is a spatial representation of the optical path difference (OPD) between an object or area compared to a reference medium with RI n_{ref} (RI of the substrate). OPD is proportional to the difference in RI and the distance, d, light has travelled as

$$OPD(x, y) = d * (n(x, y) - n_{ref}) \qquad (5-2)$$

Where $n(x, y)$ designates the local RI of the object or area of interest. Note here that in a CGM setup operated in reflection mode, such as the one schematically presented in figure 5-8 a), d corresponds to twice the thickness of the imaged object.
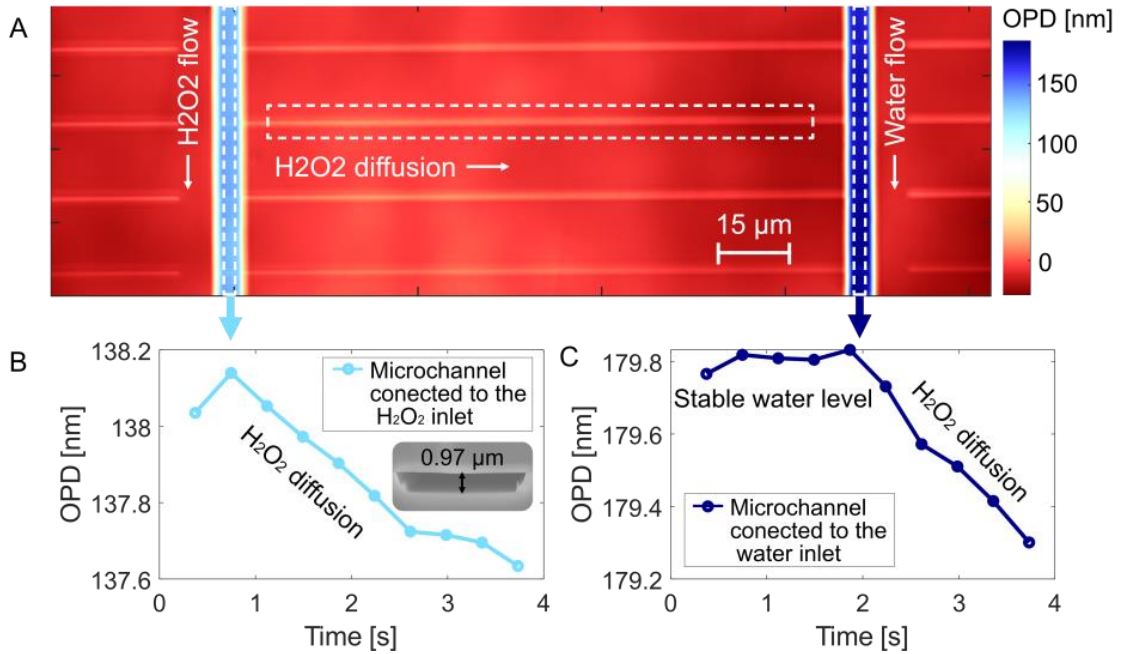

Figure 5-9. a) Wavefront image of two microfluidic channels connected by an array of parallel nanochannels. The microchannel on the left is connected to a reservoir with a 30 % H_2O_2 solution, and the microchannel on the right is filled with pure water. Dynamic tracking of the average OPD in the areas marked by dashed lines in a) reveals an increase of H_2O_2 concentration occurring at a different point in time for the channel on the left (b) and the one on the right (c). The microfluidic channel dimensions are depicted in the inset in b).

Figure 5-9 shows a wavefront image of one of my fluidic systems. First focusing on the microfluidic channels, they appear vertically across the OPD image and have identical physical dimensions but are filled with different

liquids, i.e., water ($n = 1.332$) on the right side and ~30 % H_2O_2 ($n = 1.352$) on the left. Therefore, they exhibit different OPD values and appear in different tints of blue in the image. Thermally oxidized silicon constitutes the reference material with RI $n_{ref} = 1.46$[104]. In a time series measurement, OPD changes can thus be tracked to monitor the flow of a liquid through a fluidic system and a change in RI of the liquid can be detected as a change in OPD. In figure 5-9 b) an example is depicted in which I increase the RI of the liquid in the system by letting a 30 % H_2O_2 solution hosted in one of the microchannels diffuse into the water-filled nanochannels.

Turning our attention to the nanofluidic channels, since they are diffraction-limited, the OPD change associated with the optical volume ($OV = nV$) of a nanochannel is smeared out by the PSF of the system. However, as one of the key conclusions from my thesis work, by integrating the OPD signal over an area S, containing the optical smeared out signal, it is still possible to obtain meaningful measurements of optical volume differences[123] (OVD) also from nanofluidic channels:

$$OVD = \iint_S OPD(x,y)dxdy \qquad (5-3)$$

From the OVD obtained by this integration, the RI of the liquid inside the nanochannel can be extracted by dividing the OVD with the physical volume of the analyzed nanochannel section.

Figure 5-10 exemplifies how this strategy can be used to extract quantitative RI changes in nanochannels of different dimensions. As expected, larger channels, as well as larger RI shifts with regard to the reference material, yield larger wavefront distortions and thus OVD. A more detailed description

of the data treatment and the possibilities and limitations of the technique are presented in Manuscript II.
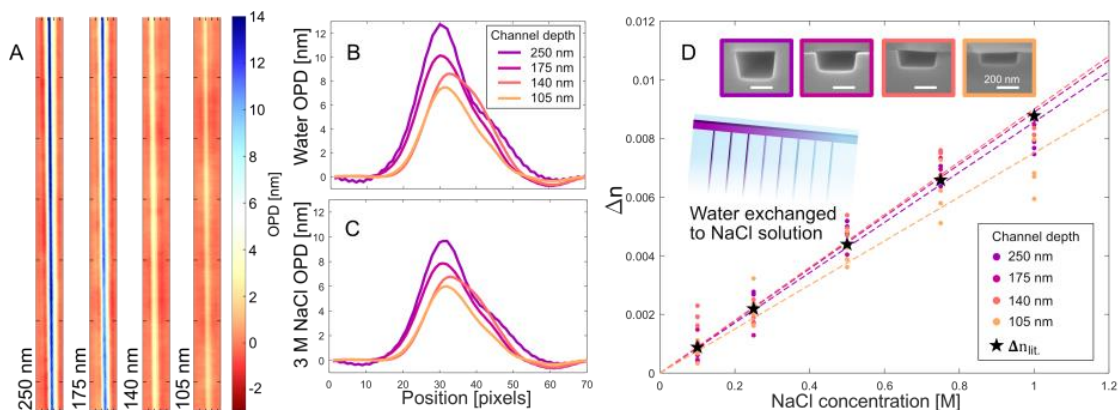

Figure 510. Wavefront images of nanofluidic channels (350 nm wide) with 4 different depths indicated in the figure are shown in a). The background is removed in each image. The same 4 channels filled with water (b) result in OPD profiles with larger peak OPD values than when they are filled with NaCl solution (c), since water has a larger RI difference to the reference medium (silica). The OVD can subsequently be calculated by integrating the OPD profiles in b) and c) and then converted into RI difference by division with the physical volume of the nanochannels, as displayed in d) (see inset for nanochannel cross section SEM images used to calculate the cross section). The calculated RI difference between a channel filled with water and NaCl solution, respectively, is displayed in d) for different NaCl concentrations. The black markers ($\star$) indicate the literature values, and the circular markers ($\cdot$) represent measurements of individual channels, where the color represents the channel dimensions. The dashed lines display a linear fit to the data presented in the same color.

Several methods for determining the concentration of a solute in nanochannels have been reported in the literature. These methods typically rely on so-called *calibration curves*, i.e., graphs that relate the measurement signal to known concentrations of solutes in a channel.[96,124–129] Such a

calibration curve was presented for my dark-field scattering based measurements in figure 5-3 d), where the scattering intensity was found to be linearly dependent on the concentration of NaCl solution within the nanochannels. For comparison, I also constructed such a calibration curve for CGM in the following way: I first extract the OVD of an arbitrary section of the channel from two separate measurements and subsequently divide it with the physical volume of the channel to retrieve the RI difference as

$$\Delta n = \frac{OVD_{NaCl} - OVD_{water}}{V} \qquad (5-4)$$

where $V = A * L$, is the volume of the object, of length L and cross-sectional area A, captured within the image. A can be determined by SEM analysis, and L is deduced by the number of included image pixels and the magnification of the system. This approach was employed to construct the curve relating Δn and NaCl concentration, presented in figure 5-10 d). However, this calculation provides the actual RI shift when the liquid inside the channel is exchanged and can therefore be considered a quantitative measurement. Consequently, the graph in figure 5-10 d) serves more as an indication of the sensitivity of the method, rather than a conventional calibration curve.

To further investigate the resolution of CGM in terms of RI measurements inside nanofluidic channels, I also examined a set of smaller nanochannels, with cross-sectional dimensions of 90×90 nm², as shown in figure 5-11 c). With the configuration used within the experiment and the appurtenant data analysis procedure, the accuracy of the Δn measurement of these channels (in regard to expected literature values) was considerably lower compared to

larger channels (e.g. 250×350 nm²). This can be explained by their respective differences in OPD contrast, see figure 5-11 a-b). As can be observed, the signal to noise ratio is much lower in figure 5-11 b) and thus yields lower Δn sensitivity.
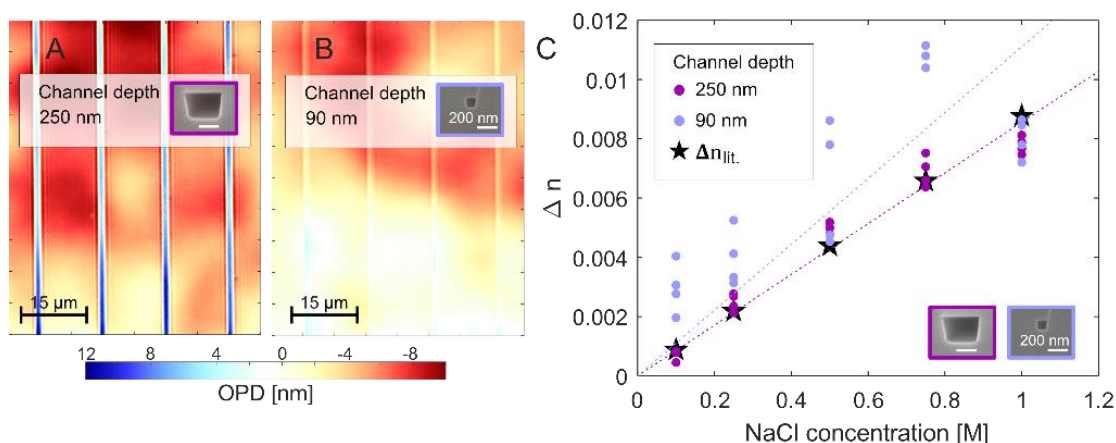

Figure 5-81. Wavefront images of nanochannels of 250×350 nm² (a), and 90×90 nm² (b), filled with water are displayed. The insets display an SEM image of the respective channel cross section with a scale bar of 200 nm. c) Measured RI difference between a channel filled with water and NaCl solution, for different NaCl concentrations. The black markers (⋆) indicate the literature values for RI difference, and the circular markers (·) represent measurements of individual channels, where the color represents the channel dimensions. The dashed lines display a linear fit to the data presented in the same color.

The measurements presented in figure 5-11 c) are performed on the same channels as depicted in figure 5-3 d) for dark-field microscopy measurement, which displayed a lower background noise. The background signals in wavefront images measured with CGM have multiple origins, where the most influential factors concern wavefront alignment between the sample and reference interferogram, and heterogeneities of RI in either the

borosilicate lid or within the thermalized layer of the silicon chip. Another factor that determines the precision of Δn measurements with CGM is the accuracy with which the nanochannel cross section has been determined. As evident from equation 5-4, the accuracy of the used channel cross section area A is critical for predicting the correct RI as the OV is directly proportional to the physical volume of the nanochannel. Therefore, in my work, I have conducted cross-sectional SEM imaging of nanochannels fabricated on the same wafer as the chip used for my experiments (see e.g. inset in Figure 5-11).

6 Conclusions, Reflections and Outlook

In this thesis, I have shown that both dark-field scattering microscopy and CGM can be used for monitoring RI changes of a liquid within nanofluidic channels. One of the key promises of CGM lies in its quantitative measurement capability, i.e., that when the physical volume of a channel is known, a single measurement can yield an *absolute* RI value and not only a relative change. Additionally, CGM enables the simultaneous analysis of fluidic channels on multiple length scales, as the spatial resolution of the interferogram supports parallel imaging in a large field of view. In contrast, dark-field scattering microscopy is less suited for measuring RI changes in microfluidic channels, as scattering intensity signals solely can be detected at the channel walls. Although such measurements can be employed to indicate the presence of a liquid exchange, they do not yield direct information about RI changes away from the wall of the microchannel.

In principle, the limit of detection for both methods is governed by photon flux, and systems equipped with a strong light source and fast cameras can therefore substantially push sensitivity. Nonetheless, in the studies presented within this thesis, dark-field scattering microscopy consistently reached higher resolution in terms of detectable RI changes in practice, as illustrated by a comparison between Figure 5-4 d) (dark-field) and Figure 5-11 c) (CGM). Respective measurements were acquired with similar cameras and exposure time settings. Part of this advantage stems from the lower background noise in dark-field microscopy and simplicity in setup that does not impose stringent requirements on light coherence or bandwidth. In contrast, CGM is limited to narrowband, non-coherent light sources. Another consideration is robustness to experimental alignment. Dark-field scattering

tolerates minor sample tilts without compromising measurement accuracy, whereas CGM is more vulnerable in this respect. Small tilts can introduce phase shifts between reference and measurement interferograms, degrading quantitative accuracy. In this work, we addressed this limitation by comparing subsequently acquired interferograms of a channel filled with two different liquids to obtain the RI difference between the two liquids, effectively eliminating phase shifts induced by sample tilt. While this strategy successfully preserved relative RI sensitivity, it did not offer clear advantages over dark-field scattering in the specific context of monitoring nanochannel content alone.

However, CGM holds unique promise in other areas. For instance, in nanoparticle tracking within microfluidic systems, I believe CGM could provide dual insight: integrated measurements spanning the full extent of a PSF (OVD measurements) may be used to track RI changes in the particle itself, while OPD simultaneously reflects variations in the surrounding medium. The ability of bridging length scales and its quantitative nature makes CGM therefore a valuable complement to dark-field scattering microscopy.

Other key findings presented in this thesis and in Manuscript I are the analysis of scattering of light from metal nanoparticles localized in a nanotrench. By imaging nanodisks and trenches of different sizes, dramatic changes in the scattering intensity relative to the trench were observed, i.e., a difference of only 10 nm in diameter between particles resulted in the particle appearing bright or dark. Similarly, it was shown that the relative scattering intensity of a particle-trench response from a diffraction limited spot is highly dependent on the illumination angle and wavelength, as well

as the dielectric functions of the respective materials within that spot. Although alterations of size, shape, and material of a system are expected to influence its optical response, I was surprised at the extent of observed variations, especially the recorded inversion of optical contrast induced by miniscule changes of the system.

For future studies, it would be interesting to further investigate dynamic shifts in scattering response, for example; employ nanofluidic scattering microscopy to monitor processes, such as growth of colloidal particles in a nanochannel, adsorption of surfactants on plasmonic particles, or even probe particle surface reconstructions during catalysis, depending on the sensitivity of the microscope, and capability of the nanofluidic platform. In such studies, the theoretical framework presented in chapter 4 could be helpful for qualitatively interpretating shifts in relative scattering intensity. In addition, the insights from both theory and experiment with size gradient arrays of particles can be used to tune visibility of metal particles in nanofluidic channels.

Acknowledgments

References

1. Taylor, A. B. & Zijlstra, P. Single-Molecule Plasmon Sensing: Current Status and Future Prospects. *ACS Sensors* **2**, 1103–1122 (2017).

2. Qian, X.-M. & Nie, S. M. Single-molecule and single-nanoparticle SERS: from fundamental mechanisms to biomedical applications. *Chem. Soc. Rev.* **37**, 912–920 (2008).

3. Bustamante, C. J., Chemla, Y. R., Liu, S. & Wang, M. D. Optical tweezers in single-molecule biophysics. *Nat. Rev. Methods Prim.* **1**, 25 (2021).

4. De Vlaminck, I. & Dekker, C. Recent advances in magnetic tweezers. *Annu. Rev. Biophys.* **41**, 453–472 (2012).

5. McDowell, M. T. *et al.* In Situ TEM of Two-Phase Lithiation of Amorphous Silicon Nanospheres. *Nano Lett.* **13**, 758–764 (2013).

6. Cheng, Y., Grigorieff, N., Penczek, P. A. & Walz, T. A Primer to Single-Particle Cryo-Electron Microscopy. *Cell* **161**, 438–449 (2015).

7. Frank, J. Advances in the field of single-particle cryo-electron microscopy over the last decade. *Nat. Protoc.* **12**, 209–212 (2017).

8. Dekker, C. Solid-state nanopores. *Nat. Nanotechnol.* **2**, 209–215 (2007).

9. Valeur, B. & Berberan-Santos, M. N. *Molecular Fluorescence: Principles and Applications*. (John Wiley & Sons, 2013).

10. Zhou, X. *et al.* Quantitative super-resolution imaging uncovers reactivity patterns on single nanocatalysts. *Nat. Nanotechnol.* **7**, 237–241 (2012).

11. van Schrojenstein Lantman, E. M., Deckert-Gaudig, T., Mank, A. J. G., Deckert, V. & Weckhuysen, B. M. Catalytic processes monitored at the nanoscale with tip-enhanced Raman spectroscopy. *Nat. Nanotechnol.* **7**, 583–586 (2012).

12. Novo, C., Funston, A. M. & Mulvaney, P. Direct observation of chemical reactions on single gold nanocrystals using surface plasmon spectroscopy. *Nat. Nanotechnol.* **3**, 598–602 (2008).

13. Mayer, K. M., Hao, F., Lee, S., Nordlander, P. & Hafner, J. H. A single molecule immunoassay by localized surface plasmon

resonance. *Nanotechnology* **21**, 255503 (2010).

14. Zhong, J. *et al.* Exploring Anomalous Fluid Behavior at the Nanoscale: Direct Visualization and Quantification via Nanofluidic Devices. *Acc. Chem. Res.* (2020) doi:10.1021/acs.accounts.9b00411.

15. Wang, M., Hou, Y., Yu, L. & Hou, X. Anomalies of Ionic/Molecular Transport in Nano and Sub-Nano Confinement. *Nano Lett.* **20**, 6937–6946 (2020).

16. Nazari, M., Davoodabadi, A., Huang, D., Luo, T. & Ghasemi, H. On interfacial viscosity in nanochannels. *Nanoscale* **12**, 14626–14635 (2020).

17. Chen, W. Q., Sedighi, M. & Jivkov, A. P. Thermo-osmosis in hydrophilic nanochannels: Mechanism and size effect. *Nanoscale* **13**, 1696–1716 (2021).

18. Robin, P. & Bocquet, L. Nanofluidics at the crossroads. *J. Chem. Phys.* **158**, 160901 (2023).

19. Zhu, Z., Wang, D., Tian, Y. & Jiang, L. Ion/Molecule Transportation in Nanopores and Nanochannels: From Critical Principles to Diverse Functions. *J. Am. Chem. Soc.* **141**, 8658–8669 (2019).

20. Albinsson, D. *et al.* Operando detection of single nanoparticle activity dynamics inside a model pore catalyst material. *Sci. Adv.* **6**, eaba7678–eaba7678 (2020).

21. Levin, S. *et al.* Nanofluidic Trapping of Faceted Colloidal Nanocrystals for Parallel Single-Particle Catalysis. *ACS Nano* (2022) doi:10.1021/acsnano.2c06505.

22. Altenburger, B. *et al.* Label-Free Imaging of Catalytic H2O2 Decomposition on Single Colloidal Pt Nanoparticles Using Nanofluidic Scattering Microscopy. *ACS Nano* **17**, 21030–21043 (2023).

23. Hur, J. & Chung, A. J. Microfluidic and Nanofluidic Intracellular Delivery. *Adv. Sci.* **8**, 2004595 (2021).

24. Yin, D. *et al.* A battery-free nanofluidic intracellular delivery patch for internal organs. *Nature* (2025) doi:10.1038/s41586-025-08943-x.

25. Schoch, R. B., Han, J. & Renaud, P. Transport phenomena in nanofluidics. *Rev. Mod. Phys.* **80**, 839–883 (2008).

26. Bocquet, L. & Charlaix, E. Nanofluidics, from bulk to interfaces.

Chem. Soc. Rev. **39**, 1073–1095 (2010).

27. Harms, Z. D. *et al.* Single-Particle Electrophoresis in Nanochannels. *Anal. Chem.* **87**, 699–705 (2015).

28. Calado, M. R. C. *et al.* Nanofluidic resistive pulse sensing for characterization of extracellular vesicles. *Lab Chip* **24**, 4028–4038 (2024).

29. Albinsson, D. *et al.* Operando detection of single nanoparticle activity dynamics inside a model pore catalyst material. *Sci. Adv.* **6**, eaba7678–eaba7678 (2020).

30. Shimizu, H., Toyoda, K., Mawatari, K., Terabe, S. & Kitamori, T. Femtoliter Gradient Elution System for Liquid Chromatography Utilizing Extended Nanofluidics. *Anal. Chem.* **91**, 3009–3014 (2019).

31. Yesibolati, M. N. *et al.* Unhindered Brownian Motion of Individual Nanoparticles in Liquid-Phase Scanning Transmission Electron Microscopy. *Nano Lett.* **20**, 7108–7115 (2020).

32. Zand, K., Pham, T., Davila, A. J., Wallace, D. C. & Burke, P. J. Nanofluidic Platform for Single Mitochondria Analysis Using Fluorescence Microscopy. *Anal. Chem.* **85**, 6018–6025 (2013).

33. Müller, V. & Westerlund, F. Optical DNA mapping in nanofluidic devices: principles and applications. *Lab Chip* **17**, 579–590 (2017).

34. Vira, S., Mekhedov, E., Humphrey, G. & Blank, P. S. Fluorescent-labeled antibodies: Balancing functionality and degree of labeling. *Anal. Biochem.* **402**, 146–150 (2010).

35. Toseland, C. P. Fluorescent labeling and modification of proteins. *J. Chem. Biol.* **6**, 85–95 (2013).

36. Lee, T., Senyuk, B., Trivedi, R. P. & Smalyukh, I. I. Optical Microscopy of Soft Matter Systems. in *Fluids, Colloids and Soft Materials* 165–185 (2016). doi:https://doi.org/10.1002/9781119220510.ch10.

37. Gage, S. H. Modern Dark-Field Microscopy and the History of Its Development. *Trans. Am. Microsc. Soc.* **39**, 95–141 (1920).

38. Kukura, P. *et al.* High-speed nanoscopic tracking of the position and orientation of a single virus. *Nat. Methods* **6**, 923–927 (2009).

39. Špačková, B. *et al.* Label-free nanofluidic scattering microscopy of size and mass of single diffusing molecules and nanoparticles. *Nat.*

Methods **19**, 751–758 (2022).

40. Levin, S. *et al.* Nanofluidic Trapping of Faceted Colloidal Nanocrystals for Parallel Single-Particle Catalysis. *ACS Nano* **16**, 15206–15214 (2022).

41. Altenburger, B., Fritzsche, J. & Langhammer, C. Femtoliter Batch Reactors for Nanofluidic Scattering Spectroscopy Analysis of Catalytic Reactions on Single Nanoparticles. *Small Methods* **n/a**, 2500693 (2025).

42. Barer, R. & Joseph, S. Refractometry of living cells part I. basic principles. *J. Cell Sci.* **s3-95**, 399–423 (1954).

43. Maier, S. A. Plasmonics: Fundamentals And Applications. in 245 (2007).

44. Langhammer, C., Yuan, Z., Zorić, I. & Kasemo, B. Plasmonic Properties of Supported Pt and Pd Nanostructures. *Nano Lett.* **6**, 833–838 (2006).

45. Langhammer, C., Kasemo, B. & Zorić, I. Absorption and scattering of light by Pt, Pd, Ag, and Au nanodisks: Absolute cross sections and branching ratios. *J. Chem. Phys.* **126**, (2007).

46. Zorić, I., Zäch, M., Kasemo, B. & Langhammer, C. Gold, Platinum, and Aluminum Nanodisk Plasmons: Material Independence, Subradiance, and Damping Mechanisms. *ACS Nano* **5**, 2535–2546 (2011).

47. Chaumet, P. C., Bon, P., Maire, G., Sentenac, A. & Baffou, G. Quantitative phase microscopies: accuracy comparison. *Light Sci. Appl.* **13**, 288 (2024).

48. Bon, P., Maucort, G., Wattellier, B. & Monneret, S. Quadriwave lateral shearing interferometry for quantitative phase microscopy of living cells. *Opt. Express* **17**, 13080 (2009).

49. Bénéfice, M. *et al.* Dry mass photometry of single bacteria using quantitative wavefront microscopy. *Biophys. J.* **122**, 3159–3172 (2023).

50. Baffou, G. Wavefront Microscopy Using Quadriwave Lateral Shearing Interferometry: From Bioimaging to Nanophotonics. *ACS Photonics* **10**, 322–339 (2023).

51. Bianco, V. *et al.* Endowing a plain fluidic chip with micro-optics: a holographic microscope slide. *Light Sci. Appl.* **6**, e17055–e17055

(2017).

52. Jang, J., Bae, C. Y., Park, J.-K. & Ye, J. C. Self-reference quantitative phase microscopy for microfluidic devices. *Opt. Lett.* **35**, 514–516 (2010).

53. Sung, Y. *et al.* Three-Dimensional Holographic Refractive-Index Measurement of Continuously Flowing Cells in a Microfluidic Channel. *Phys. Rev. Appl.* **1**, 14002 (2014).

54. Roitshtain, D. *et al.* Quantitative phase microscopy spatial signatures of cancer cells. *Cytom. Part A* **91**, 482–493 (2017).

55. Luo, Y. *et al.* Three-dimensional visualization and analysis of flowing droplets in microchannels using real-time quantitative phase microscopy. *Lab Chip* **21**, 75–82 (2021).

56. Luo, Y. *et al.* Dispersive phase microscopy incorporated with droplet-based microfluidics for biofactory-on-a-chip. *Lab Chip* **23**, 2766–2777 (2023).

57. Craighead, H. G. Nanoelectromechanical Systems. *Science (80-.).* **290**, 1532–1535 (2000).

58. Eijkel, J. C. T. & Berg, A. van den. Nanofluidics: what is it and what can we expect from it? *Microfluid. Nanofluidics* **1**, 249–267 (2005).

59. Xu, Y. Nanofluidics: A New Arena for Materials Science. *Adv. Mater.* **30**, 1702419 (2018).

60. Napoli, M., Eijkel, J. C. T. & Pennathur, S. Nanofluidic technology for biomolecule applications: a critical review. *Lab Chip* **10**, 957–985 (2010).

61. Whitesides, G. M. The origins and the future of microfluidics. *Nature* **442**, 368–373 (2006).

62. Hu, Z.-L., Huo, M.-Z., Ying, Y.-L. & Long, Y.-T. Biological Nanopore Approach for Single-Molecule Protein Sequencing. *Angew. Chemie Int. Ed.* **60**, 14738–14749 (2021).

63. Coquinot, B. *et al.* Momentum tunnelling between nanoscale liquid flows. *Nat. Nanotechnol.* **20**, 397–403 (2025).

64. Kavokine, N., Bocquet, M.-L. & Bocquet, L. Fluctuation-induced quantum friction in nanoscale water flows. *Nature* **602**, 84–90 (2022).

65. Harms, Z. D., Selzer, L., Zlotnick, A. & Jacobson, S. C. Monitoring Assembly of Virus Capsids with Nanofluidic Devices. *ACS Nano* **9**,

9087–9096 (2015).

66. Faez, S. *et al.* Fast, Label-Free Tracking of Single Viruses and Weakly Scattering Nanoparticles in a Nanofluidic Optical Fiber. *ACS Nano* **9**, 12349–12357 (2015).

67. Mitra, A., Deutsch, B., Ignatovich, F., Dykes, C. & Novotny, L. Nano-optofluidic detection of single viruses and nanoparticles. *ACS Nano* **4**, 1305–1312 (2010).

68. Nakao, T. *et al.* Cytokine analysis on a countable number of molecules from living single cells on nanofluidic devices. *Analyst* **144**, 7200–7208 (2019).

69. Li, Y. *et al.* Engineering a Smart Nanofluidic Sensor for High-Performance Peroxynitrite Sensing through a Spirocyclic Ring Open/Close Reaction Strategy. *ACS Sensors* **6**, 808–814 (2021).

70. Ronceray, N. *et al.* Liquid-activated quantum emission from pristine hexagonal boron nitride for nanofluidic sensing. *Nat. Mater.* **22**, 1236–1242 (2023).

71. Hou, Y. & Hou, X. Bioinspired nanofluidic iontronics. *Science (80-.).* **373**, 628–629 (2021).

72. Emmerich, T. *et al.* Nanofluidic logic with mechano–ionic memristive switches. *Nat. Electron.* **7**, 271–278 (2024).

73. Portillo, S., Ramirez, P., Mafe, S. & Cervera, J. Neuromorphic Reservoir Computing with Memristive Nanofluidic Diodes. *Nano Lett.* (2025) doi:10.1021/acs.nanolett.5c00853.

74. Feng, J. *et al.* Single-layer MoS2 nanopores as nanopower generators. *Nature* **536**, 197–200 (2016).

75. Zhang, Z., Wen, L. & Jiang, L. Nanofluidics for osmotic energy conversion. *Nat. Rev. Mater.* **6**, 622–639 (2021).

76. Xin, W., Jiang, L. & Wen, L. Two-Dimensional Nanofluidic Membranes toward Harvesting Salinity Gradient Power. *Acc. Chem. Res.* **54**, 4154–4165 (2021).

77. Yu, R.-J., Ying, Y.-L., Gao, R. & Long, Y.-T. Confined Nanopipette Sensing: From Single Molecules, Single Nanoparticles, to Single Cells. *Angew. Chemie Int. Ed.* **58**, 3706–3714 (2019).

78. Tunuguntla, R. H. *et al.* Enhanced water permeability and tunable ion selectivity in subnanometer carbon nanotube porins. *Science (80-.).*

357, 792–796 (2017).

79. Raidongia, K. & Huang, J. Nanofluidic Ion Transport through Reconstructed Layered Materials. *J. Am. Chem. Soc.* **134**, 16528–16531 (2012).

80. Koltonow, A. R. & Huang, J. Two-dimensional nanofluidics. *Science (80-.).* **351**, 1395–1396 (2016).

81. Radha, B. *et al.* Molecular transport through capillaries made with atomic-scale precision. *Nature* **538**, 222–225 (2016).

82. Chou, S. Y., Krauss, P. R., Zhang, W., Guo, L. & Zhuang, L. Sub-10 nm imprint lithography and applications. *J. Vac. Sci. Technol. B Microelectron. Nanom. Struct. Process. Meas. Phenom.* **15**, 2897–2904 (1997).

83. Quake, S. R. & Scherer, A. From Micro- to Nanofabrication with Soft Materials. *Science (80-.).* **290**, 1536–1540 (2000).

84. Cai, Z., Liu, B., Zou, X. & Cheng, H.-M. Chemical Vapor Deposition Growth and Applications of Two-Dimensional Materials and Their Heterostructures. *Chem. Rev.* **118**, 6091–6133 (2018).

85. Xia, Y. & Whitesides, G. M. Soft lithography. *Angew. Chemie Int. Ed.* **37**, 550–575 (1998).

86. Biswas, A. *et al.* Advances in top–down and bottom–up surface nanofabrication: Techniques, applications & future prospects. *Adv. Colloid Interface Sci.* **170**, 2–27 (2012).

87. Fritzsche, J. *et al.* Single Particle Nanoplasmonic Sensing in Individual Nanofluidic Channels. *Nano Lett.* **16**, 7857–7864 (2016).

88. Levin, S. *et al.* A nanofluidic device for parallel single nanoparticle catalysis in solution. *Nat. Commun.* **10**, 4426 (2019).

89. Albinsson, D. *et al.* Operando detection of single nanoparticle activity dynamics inside a model pore catalyst material. *Sci. Adv.* **6**, eaba7678–eaba7678 (2020).

90. Rathnayaka, C. *et al.* Nanofluidic devices for the separation of biomolecules. *J. Chromatogr. A* **1683**, 463539 (2022).

91. Niculescu, A.-G., Chircov, C., Bîrcă, A. C. & Grumezescu, A. M. Fabrication and Applications of Microfluidic Devices: A Review. *International Journal of Molecular Sciences* vol. 22 at https://doi.org/10.3390/ijms22042011 (2021).

92.   Nielsen, J. B. *et al.* Microfluidics: Innovations in Materials and Their Fabrication and Functionalization. *Anal. Chem.* **92**, 150–168 (2020).

93.   Hwang, J., Cho, Y. H., Park, M. S. & Kim, B. H. Microchannel Fabrication on Glass Materials for Microfluidic Devices. *Int. J. Precis. Eng. Manuf.* **20**, 479–495 (2019).

94.   Sinev, L. S. & Petrov, I. D. Linear Thermal Expansion Coefficient (at Temperatures from 130 to 800 K) of Borosilicate Glasses Suitable for Silicon Compounds in Microelectronics. *Glas. Ceram.* **73**, 32–35 (2016).

95.   Shang, L., Cheng, Y. & Zhao, Y. Emerging Droplet Microfluidics. *Chem. Rev.* **117**, 7964–8040 (2017).

96.   Altenburger, B., Fritzsche, J. & Langhammer, C. Visible Light Spectroscopy of Liquid Solutes from Femto- to Attoliter Volumes Inside a Single Nanofluidic Channel. *ACS Nano* **19**, 2857–2869 (2025).

97.   Kern, W. Cleaning solution based on hydrogen peroxide for use in silicon semiconductor technology. *RCA Rev.* **31**, 187–206 (1970).

98.   Gungor, T., Gungor, E. & Saka, B. Fast and interference fringe independent optical characterization of zinc oxide nano thin films using model-based genetic algorithm for optoelectronic applications. *Nanomater. Nanotechnol.* **6**, 1–7 (2016).

99.   Chen, Y. Nanofabrication by electron beam lithography and its applications: A review. *Microelectron. Eng.* **135**, 57–72 (2015).

100.   Laermer, F., Franssila, S., Sainiemi, L. & Kolari, K. Chapter 16 - Deep reactive ion etching. in *Micro and Nano Technologies* (eds. Tilli, M. et al.) 417–446 (Elsevier, 2020). doi:https://doi.org/10.1016/B978-0-12-817786-0.00016-5.

101.   Bohren, C. F. & Huffman, D. R. *Absorption and Scattering of Light by Small Particles*. (John Wiley & Sons, 2008).

102.   Logan, N. A. Survey of some early studies of the scattering of plane waves by a sphere. *Proc. IEEE* **53**, 773–785 (1965).

103.   Dutka, J. On the Early History of Bessel Functions. *Arch. Hist. Exact Sci.* **49**, 105–134 (1995).

104.   Malitson, I. H. Interspecimen Comparison of the Refractive Index of Fused Silica. *J. Opt. Soc. Am.* **55**, 1205–1209 (1965).

105. Asano, S. & Yamamoto, G. Light Scattering by a Spheroidal Particle. *Appl. Opt.* **14**, 29–49 (1975).

106. Kelly, K. L., Coronado, E., Zhao, L. L. & Schatz, G. C. The Optical Properties of Metal Nanoparticles: The Influence of Size, Shape, and Dielectric Environment. *J. Phys. Chem. B* **107**, 668–677 (2003).

107. Yu, R., Liz-Marzán, L. M. & García de Abajo, F. J. Universal analytical modeling of plasmonic nanoparticles. *Chem. Soc. Rev.* **46**, 6710–6724 (2017).

108. Johnson, P. B. & Christy, R. W. Optical Constants of the Noble Metals. *Phys. Rev. B* **6**, 4370–4379 (1972).

109. Werner, W. S. M., Glantschnig, K. & Ambrosch-Draxl, C. Optical Constants and Inelastic Electron-Scattering Data for 17 Elemental Metals. *J. Phys. Chem. Ref. Data* **38**, 1013–1092 (2009).

110. Hecht, E. *Optics*. (Pearson Education India, 2012).

111. Abbe, E. Beiträge zur Theorie des Mikroskops und der mikroskopischen Wahrnehmung. *Arch. für Mikroskopische Anat.* **9**, 413–468 (1873).

112. Soga, K., Umezawa, M. & Okubo, K. *Transparency in Biology: Making the Invisible Visible*. (Springer, 2020).

113. Marquet, P., Depeursinge, C. & Magistretti, P. J. Review of quantitative phase-digital holographic microscopy: promising novel imaging technique to resolve neuronal network activity and identify cellular biomarkers of psychiatric disorders. *Neurophotonics* **1**, 20901 (2014).

114. Wang, Z. *et al.* Spatial light interference microscopy (SLIM). *Opt. Express* **19**, 1016–1026 (2011).

115. Bhaduri, B. *et al.* Diffraction phase microscopy: principles and applications in materials and life sciences. *Adv. Opt. Photonics* **6**, 57–119 (2014).

116. Nguyen, T. L. *et al.* Quantitative Phase Imaging: Recent Advances and Expanding Potential in Biomedicine. *ACS Nano* **16**, 11516–11544 (2022).

117. Balasubramani, V. *et al.* Roadmap on Digital Holography-Based Quantitative Phase Imaging. *Journal of Imaging* vol. 7 at https://doi.org/10.3390/jimaging7120252 (2021).

118. Park, J.-H., Yu, Z., Lee, K., Lai, P. & Park, Y. Perspective: Wavefront shaping techniques for controlling multiple light scattering in biological tissues: Toward in vivo applications. *APL Photonics* **3**, 100901 (2018).

119. Han, Z.-G. *et al.* Determination of the laser beam quality factor (M2) by stitching quadriwave lateral shearing interferograms with different exposures. *Appl. Opt.* **56**, 7596–7603 (2017).

120. Lee, K. *et al.* Quantitative Phase Imaging Techniques for the Study of Cell Pathophysiology: From Principles to Applications. *Sensors* vol. 13 4170–4191 at https://doi.org/10.3390/s130404170 (2013).

121. Primot, J. & Guérineau, N. Extended Hartmann test based on the pseudoguiding property of a Hartmann mask completed by a phase chessboard. *Appl. Opt.* **39**, 5715–5720 (2000).

122. Khadir, S. *et al.* Full optical characterization of single nanoparticles using quantitative phase imaging. *Optica* **7**, 243–248 (2020).

123. Aknoun, S. *et al.* Living cell dry mass measurement using quantitative phase imaging with quadriwave lateral shearing interferometry: an accuracy and sensitivity discussion. *J. Biomed. Opt.* **20**, 126009 (2015).

124. Purr, F. *et al.* Asymmetric nanofluidic grating detector for differential refractive index measurement and biosensing. *Lab Chip* **17**, 4265–4272 (2017).

125. Yasui, T. *et al.* Label-free detection of real-time DNA amplification using a nanofluidic diffraction grating. *Sci. Rep.* **6**, 31642 (2016).

126. Zhao, X.-P. *et al.* Nanochannel–Ion Channel Hybrid Device for Ultrasensitive Monitoring of Biomolecular Recognition Events. *Anal. Chem.* **91**, 1185–1193 (2019).

127. Zhang, N. *et al.* Nanochannels Photoelectrochemical Biosensor. *Anal. Chem.* **90**, 2341–2347 (2018).

128. Li, X. *et al.* Neuron-Inspired Nanofluidic Biosensors for Highly Sensitive and Selective Imidacloprid Detection. *ACS Sensors* **8**, 3428–3434 (2023).

129. Tsuyama, Y. & Mawatari, K. Concentration Determination at a Countable Molecular Level in Nanofluidics by Solvent-Enhanced Photothermal Optical Diffraction. *Anal. Chem.* **92**, 14366–14372 (2020).